Disparities in particulate matter (PM_{10}) origins and oxidative potential at a city-scale (Grenoble, France) - Part I: Source apportionment at three neighbouring sites

Supplementary information

Table of Contents

S1. Positive Matrix Factorization (PMF) analyses

PMF is based on a weighted least-squares fit algorithm following Eq. S1.

$$[\text{Eq. S1}]: X = (G \times F) + E$$

where: X is an (n × m) matrix representing the species concentration (m) for each samples (n), G is the (n × p) matrix representing the source contribution, F is the (p × m) matrix representing the factor composition and E is the residuals matrix (i.e., difference between measurements and model output). A condition of non-negativity for G and F matrix is imposed by the algorithm and PMF find solutions by minimizing the sum of the squared residuals weighted by their respective uncertainties.

In order to avoid double counting, OC* was calculated using Eq. S2.

$$[\text{Eq. S2}]: OC^{*} = OC - (MSA \times 0.12) + (polyols \times 0.40) + (levoglucosan \times 0.44) + (mannosan \times 0.44)$$

The uncertainties of the input variables were calculated using Eq. S3 based on Gianini et al. (2012).

$$[\text{Eq. S3}]: \sigma_{mn} = \sqrt{(DL_m)^2 + (CV_m \times x_{mn})^2 + (a_m \times x_{mn})^2}$$

where: DL represents the species detection limit, x_{mn} represents concentration of species m on sample n, CV represents the coefficient of variation of specie m, and a_m represents an additional coefficient of variation. The calculated uncertainty of 5/6×DL was used for concentrations <DL, and the calculated uncertainty of 4 times the geometric mean was used for missing values (Polissar et al., 1998). Finally, the species chosen as input variables in the PMF matrix were evaluated based on their signal-to-noise ratio (S/N). Species with S/N>0.2 were considered as "strong", 2.0≥S/N≥0.2 were considered as "weak", and S/N<0.2 were considered as "bad".

Table S1: Summary of input variables and uncertainties in the PMF analyses.

	Carbonaceous	Water-soluble ions	Organic tracers	Metals
Species	OC*, EC	MSA, Cl^-, NO_3^-, SO_4^{2-}, NH_4^+, K^+, Mg^{2+}, Ca^{2+}	Polyols, levoglucosan, mannosan, cellulose, 3-MBTCA, phthalic acid, pinic acid	Al, As, Cd, Cr, Cu, Fe, Mn, Mo, Ni, Pb, Rb, Sb, Se, Sn, Sr, Ti, V, Zn
Uncertainties	Gianini, et al. (2012)			
factor "a"	0.03	0.05	0.10	0.15

To resolve the mixing issues, the PMF equation was solved using the ME-2 solver (Paatero, 1999; Paatero and Hopke, 2002) allowing the addition of constraints and expressions to the solved the PMF solution.

The criteria for a valid solution were the recommendations of the Joint Research Community (JRC) report based on Belis et al. (2014).

- the Q/Q_{exp} ratio (<1.5)
- the weighted residuals are normal and between ±4
- the chemical interpretation of the obtained factors
- the information based on the error estimation by bootstrap and displacement method

- the total reconstructed PM_{10} mass from the PMF-resolved factors

The solutions presented in this study are the optimal solutions from the constrained runs in each site.

The Pearson distance and the Similarity Identity Distance (PD-SID):

In order to evaluate the homogeneity of the chemical profiles in each urban site, the similarity between the factors were assessed by calculating the Pearson distance (PD) and the Similarity Identity Distance (SID), following Belis et al. (2015). The PD and SID defined by Eq. S4 and Eq. S5:

$$\text{[Eq. S4]: } PD = 1 - r^2, \text{ where r is the Pearson coefficient}$$

$$\text{[Eq. S5]: } \frac{\sqrt{2}}{n} \sum_{i=1}^{n} \frac{|a_i - b_i|}{a_i + b_i}$$

where a and b are the relative mass to PM_{10} of two different factors and n is the number of common specie in a and b. In brief, the PD-SID metric aims to compare profiles based on their relative mass composition. The PD provides information on the sensitivity of a profile to variations in the major mass fractions of PM, while the SID provides information on the sensitivity to all components. PD<0.4 and SID<1 are considered as acceptable criteria for profile similarity, according to Pernigotti and Belis (2018).

S2. PM_{10} chemical characterization

Table S2. Annual average of PM_{10} mass concentrations and chemical compositions (in µg m^3) at all sites, and individual urban sites in the Grenoble basin.

Species	All sites	CB (urban hyper-center)	LF (urban background)	Vif (peri-urban)
		µg m^{-3}		
PM_{10}	14.4 ± 9.0	16.0 ± 9.6	14.2 ± 8.3	13.1 ± 8.9
OC*	3.89 ± 2.14	4.09 ± 2.11	3.89 ± 2.03	3.7 ± 2.26
EC	1.01 ± 0.84	1.18 ± 0.89	1.12 ± 0.95	0.73 ± 0.58
Cl^-	0.12 ± 0.23	0.16 ± 0.28	0.08 ± 0.14	0.1 ± 0.23
NO_3^-	2.02 ± 2.85	2.55 ± 3.24	1.79 ± 2.53	1.72 ± 2.67
SO_4^{2-}	1.48 ± 1.01	1.58 ± 1.05	1.53 ± 1.02	1.33 ± 0.96
Na^+	0.17 ± 0.18	0.2 ± 0.22	0.15 ± 0.13	0.15 ± 0.18
NH_4^-	0.85 ± 1.05	0.99 ± 1.18	0.81 ± 0.99	0.75 ± 0.98
K^+	0.15 ± 0.12	0.16 ± 0.12	0.15 ± 0.12	0.13 ± 0.11
Mg^{2+}	0.02 ± 0.01	0.02 ± 0.02	0.02 ± 0.01	0.02 ± 0.01
Ca^{2+}	0.32 ± 0.26	0.36 ± 0.28	0.31 ± 0.26	0.3 ± 0.24
MSA	0.02 ± 0.03	0.03 ± 0.03	0.02 ± 0.03	0.02 ± 0.02
Levoglucosan	0.3 ± 0.39	0.25 ± 0.31	0.28 ± 0.35	0.36 ± 0.49
Mannosan	0.03 ± 0.04	0.03 ± 0.04	0.03 ± 0.04	0.04 ± 0.05
Polyols	0.04 ± 0.04	0.04 ± 0.04	0.04 ± 0.04	0.05 ± 0.05
Cellulose	0.08 ± 0.08	0.13 ± 0.09	0.05 ± 0.04	0.06 ± 0.07
		ng m^{-3}		
3-MBTCA	9.13 ± 9.72	9.8 ± 10.08	8.5 ± 9.21	9.09 ± 9.89
Phthalic	3.54 ± 3.48	3.5 ± 2.92	3.88 ± 4.63	3.24 ± 2.52
Pinic	6.61 ± 7.19	5.36 ± 5.79	5.25 ± 4.37	9.22 ± 9.64
Al	0.06 ± 0.09	0.06 ± 0.08	0.07 ± 0.09	0.06 ± 0.11

As	0.33 ± 0.32	0.41 ± 0.4	0.37 ± 0.31	0.23 ± 0.2
Cd	1.56 ± 2.21	2.2 ± 3.04	1.61 ± 1.8	0.86 ± 1.13
Cr	0.07 ± 0.08	0.08 ± 0.1	0.07 ± 0.08	0.05 ± 0.05
Cu	8.5 ± 7.95	11.59 ± 10.27	8.79 ± 7.24	5.09 ± 3.26
Fe	0.22 ± 0.19	0.24 ± 0.21	0.25 ± 0.2	0.16 ± 0.14
Mn	9.0 ± 14.13	11.73 ± 14.21	7.19 ± 8.08	8.03 ± 17.93
Mo	0.59 ± 0.86	0.8 ± 1.1	0.63 ± 0.89	0.35 ± 0.38
Ni	0.91 ± 0.86	1.18 ± 1.13	0.92 ± 0.74	0.63 ± 0.5
Pb	4.42 ± 5.29	5.73 ± 6.21	4.84 ± 5.64	2.69 ± 2.98
Rb	0.45 ± 0.36	0.48 ± 0.37	0.44 ± 0.34	0.41 ± 0.37
Sb	1.31 ± 4.31	1.71 ± 4.53	1.53 ± 4.83	0.69 ± 3.42
Se	0.39 ± 0.23	0.43 ± 0.23	0.41 ± 0.24	0.32 ± 0.21
Sn	2.26 ± 1.34	2.6 ± 1.48	2.45 ± 1.44	1.73 ± 0.87
Ti	3.81 ± 3.33	4.11 ± 3.26	3.83 ± 3.29	3.49 ± 3.43
V	0.48 ± 0.55	0.51 ± 0.53	0.52 ± 0.57	0.42 ± 0.55
Zn	20.25 ± 29.38	26.1 ± 33.25	23.58 ± 34.26	11.04 ± 13.89

76

S3. Error estimations, chemical profiles, and temporal evolutions of the PMF-resolved sources

Species repartition among profiles

LF

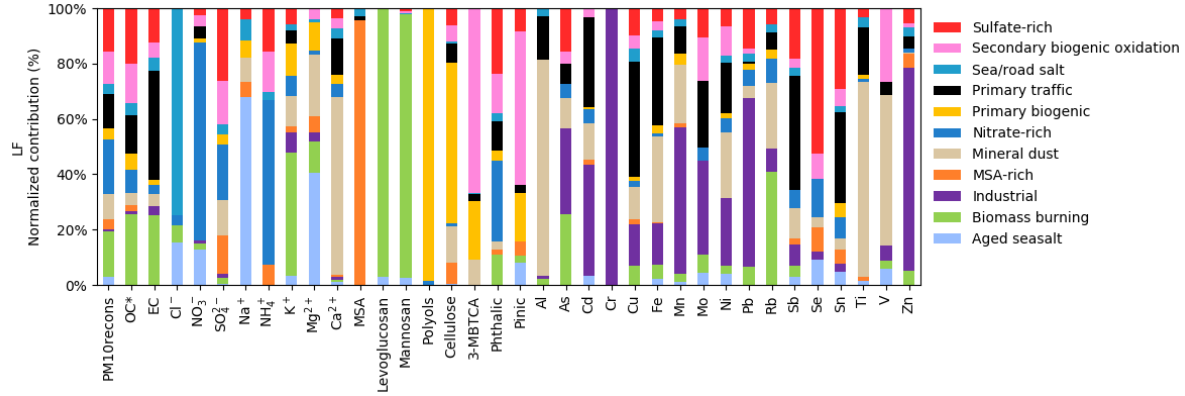

CB

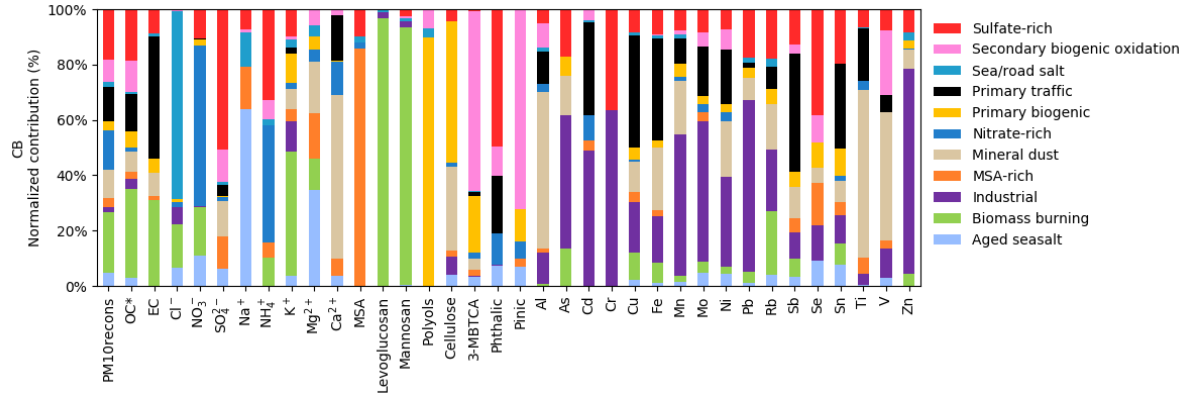

Vif

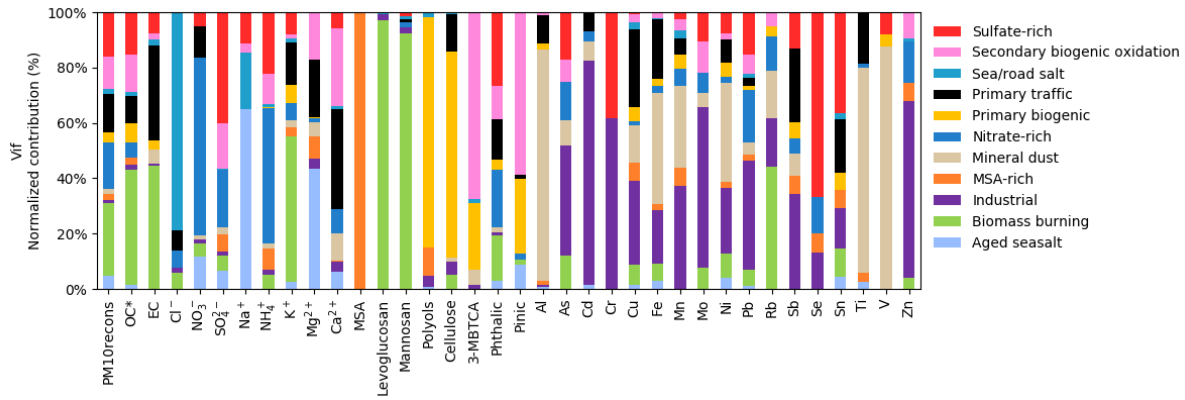

Seasonal contribution of the PMF-resolved sources to OC

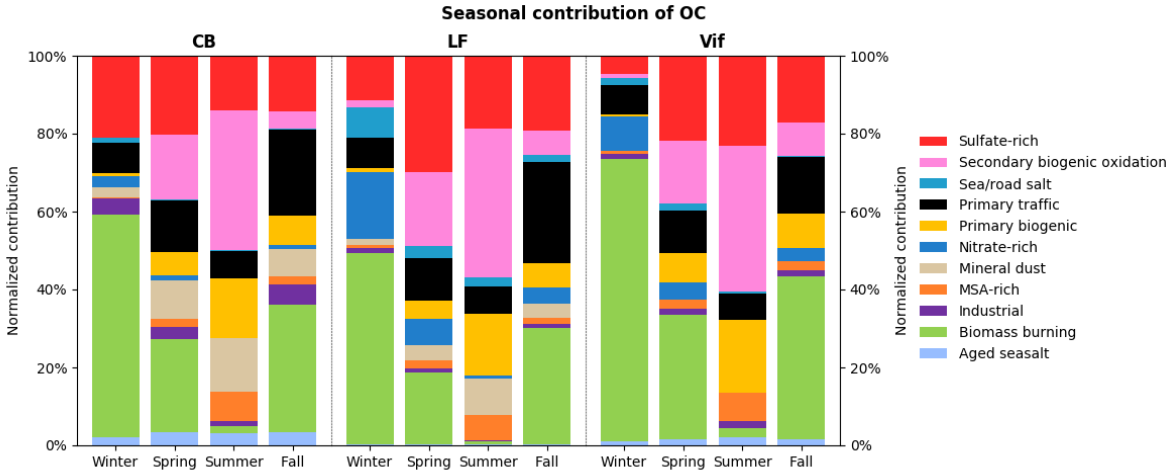

Bootstrap mapping

Table S3. Summary of the bootstrap (BS) mapping of the base and constrained run in the three urban sites.

Factor	Baseline run		Constrained run	
	Range	Mean unmapped	Range	Mean unmapped
Industrial	99-100	0	100	0
Primary biogenic	99-100	0	100	0
Biomass burning	100	0	100	0
Mineral dust	90-98	1.0	95-100	0
Sulfate-rich	75-98	1.3	88-99	0.7
Secondary biogenic oxidation	93-100	0.3	99-100	0
MSA-rich	92-96	0	100	0
Nitrate-rich	97-100	0.3	100	0
Primary traffic	93-99	0	96-100	0
Sea/road salt	79-99	0	97-100	0
Aged Sea salt	91-98	0	99-100	0

Biomass burning

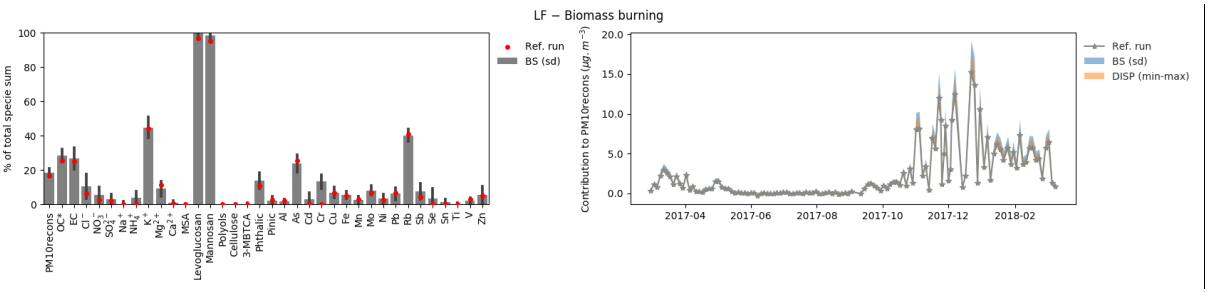

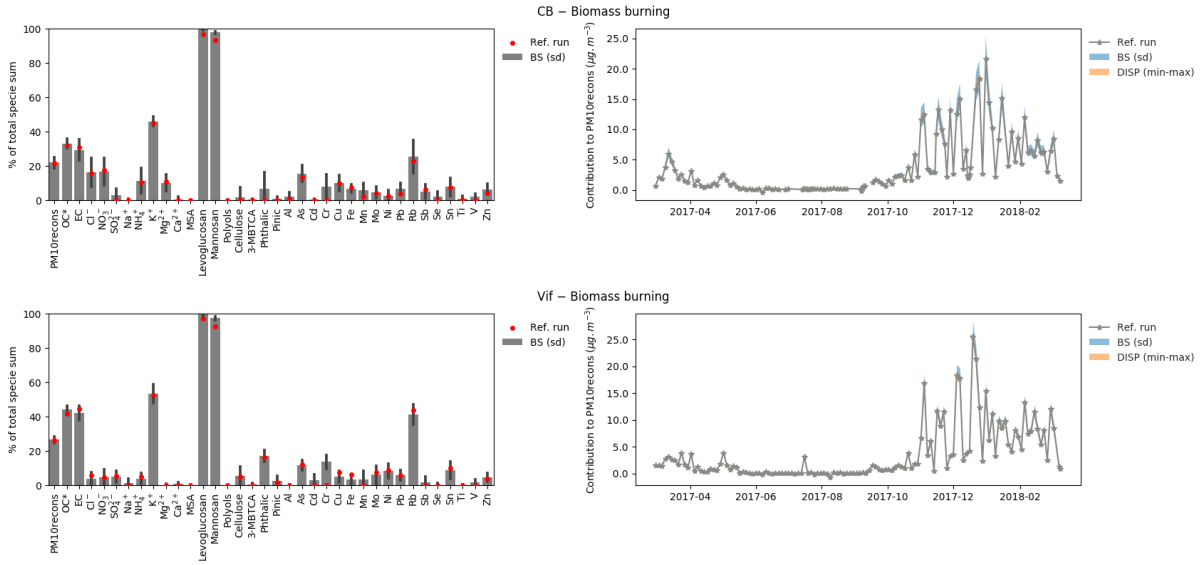

Figure S3.1. Chemical profile and temporal evolution with error estimates of the biomass burning factor in LF (top), CB (middle), and Vif (bottom).

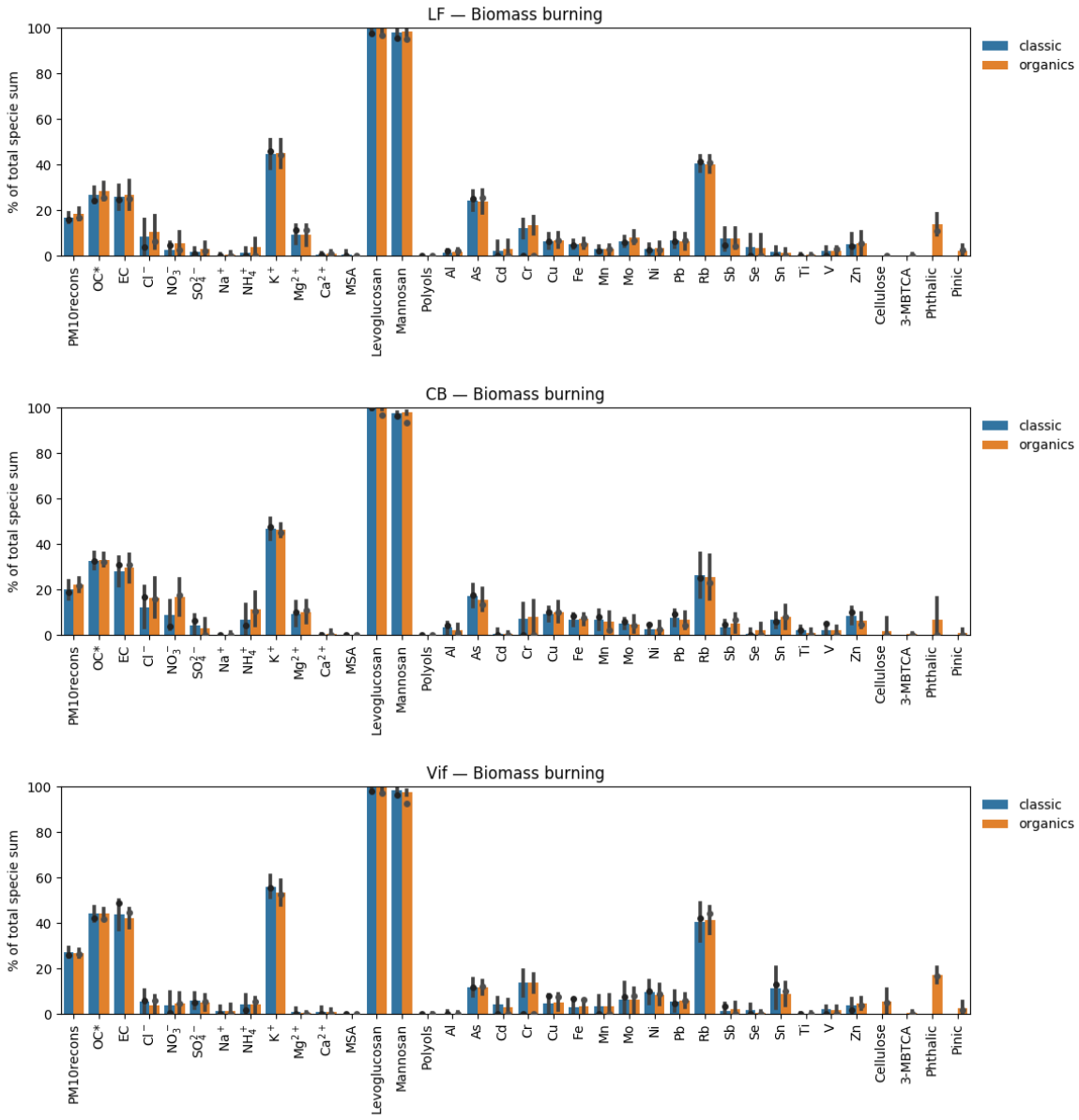

Figure S3.1.1 Comparison of chemical profile between the classic and orga PMF run for the biomass burning factor in LF (top), CB (middle), and Vif (bottom).

The biomass burning factor was identified with high loadings of levoglucosan, mannosan, K^+, and Rb. On an annual scale, biomass burning accounted for 17% (2.3 µg m^{-3}), 22% (3.5 µg m^{-3}), and 26% (3.4 µg m^{-3}) of total PM_{10} mass in LF, CB, and Vif, respectively. Strong correlations were found across all sites indicating that the influence of this factor on PM_{10} is on a larger scale. This factor also showed strong seasonality with highest contributions during the winter season, ranging according to site from 19-24% (2.2-2.5 µg m^{-3}).

In CB, a notable contribution was also observed from NO_3^- (17%) and NH_4^+ (10%) in this factor. These species are commonly associated to secondary formation processes and direct emissions from biomass burning (Tomaz et al., 2017). Aside from the usual tracers of biomass burning, contributions from phthalic acid was also seen in the LF (11%) and Vif (16%) sites. Phthalic acid is a known tracer of naphthalene-derived SOA (Al-Neima and Stone, 2017; Kleindienst et al., 2012), thereby suggesting the influence of secondary aerosols in the biomass burning factor.

Primary traffic

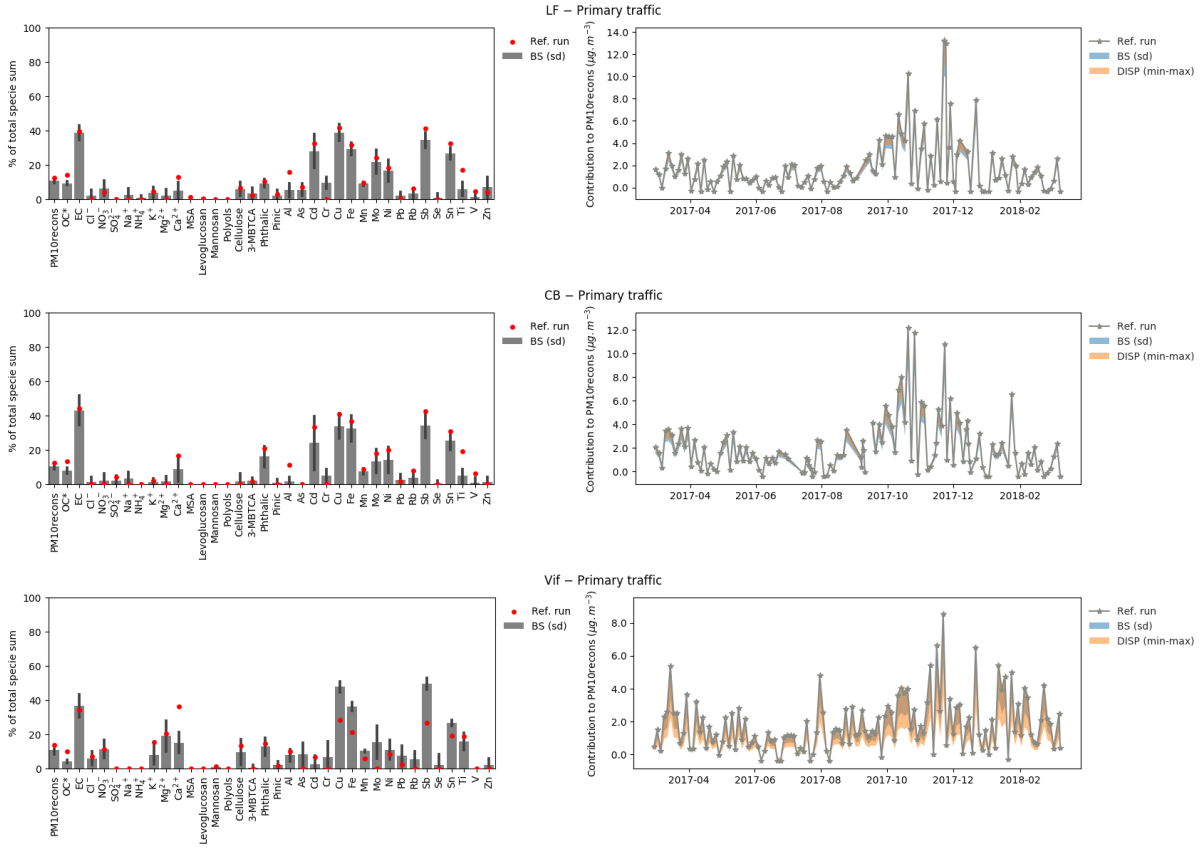

Figure S3.2. Chemical profile and temporal evolution with error estimates of the primary traffic factor in LF (top), CB (middle), and Vif (bottom).

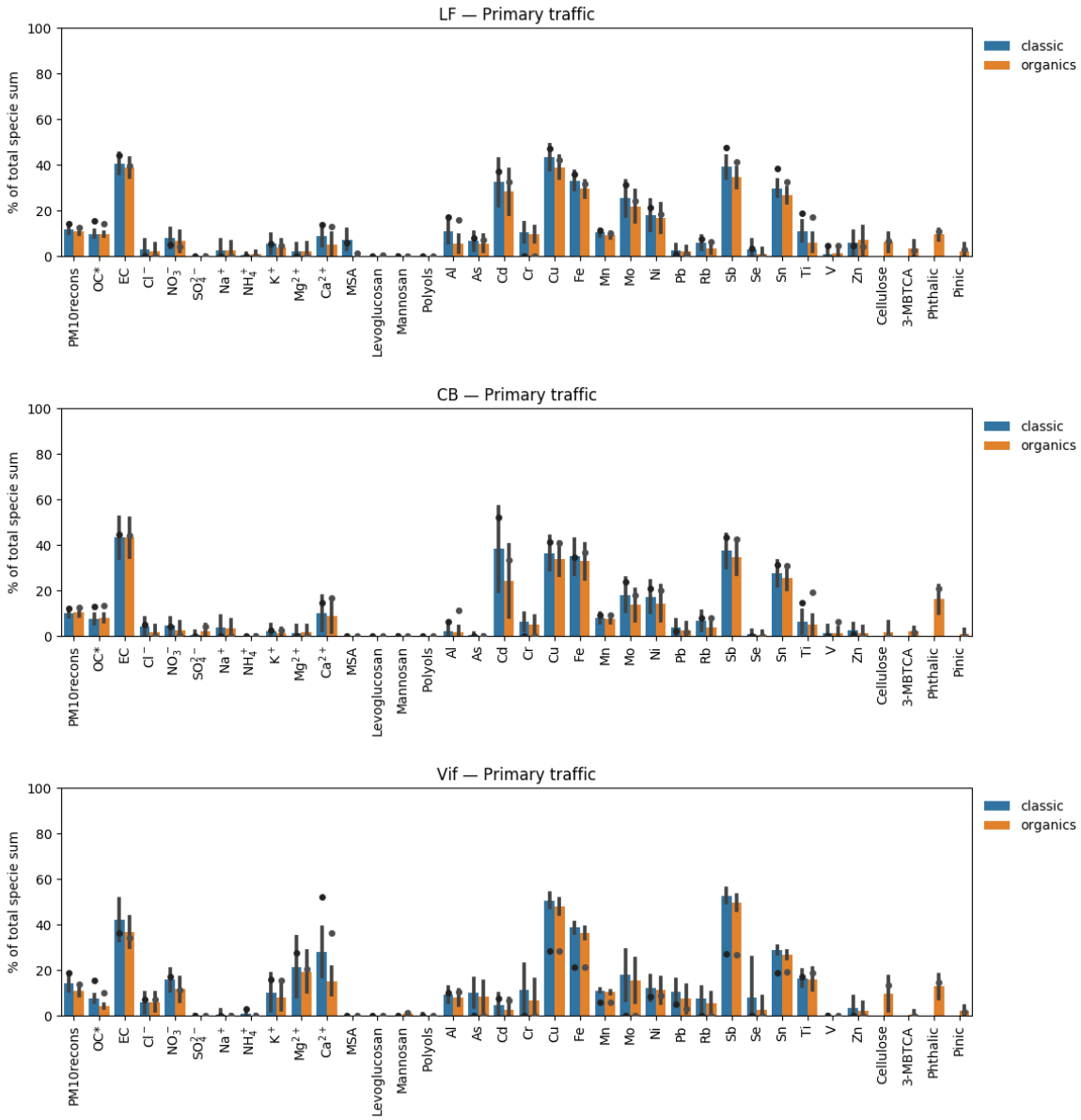

Figure S3.2.1 Comparison of chemical profile between the classic and orga PMF run for the primary traffic factor in LF (top), CB (middle), and Vif (bottom).

The primary traffic factor was identified with high loadings of EC, Cu, Fe, Sn, and Sb. On an annual scale, the primary traffic factor accounted for 11-14% in LF (1.8 µg m^{-3}), CB (2.0 µg m^{-3}), and Vif (1.8 µg m^{-3}).

A typical tracer of traffic exhaust, EC, contributed 34-44% of its total mass to the primary traffic factor. Contributions from metals in this factor can be attributed to road dust resuspension due to road traffic activity such as wear and tear of tires, brake wear, and oil burning (Kulshrestha et al., 2009; Pant and Harrison, 2013; Pant et al., 2017).

The primary traffic factor also showed minimal loadings from Cd in LF and CB sites, a tracer known to originate from urban traffic soil (Liu et al., 2007, 2011). It is also interesting to note that phthalic acid, one of the major components of automobile emissions (Kawamura and Kaplan, 1987) and a known tracer of SOA formation (Al-Neima and Stone, 2017; Kleindienst et al, 2012), has contributions to primary traffic factor ranging from 11% and 21% of its total mass in LF and CB.

Aged sea salt

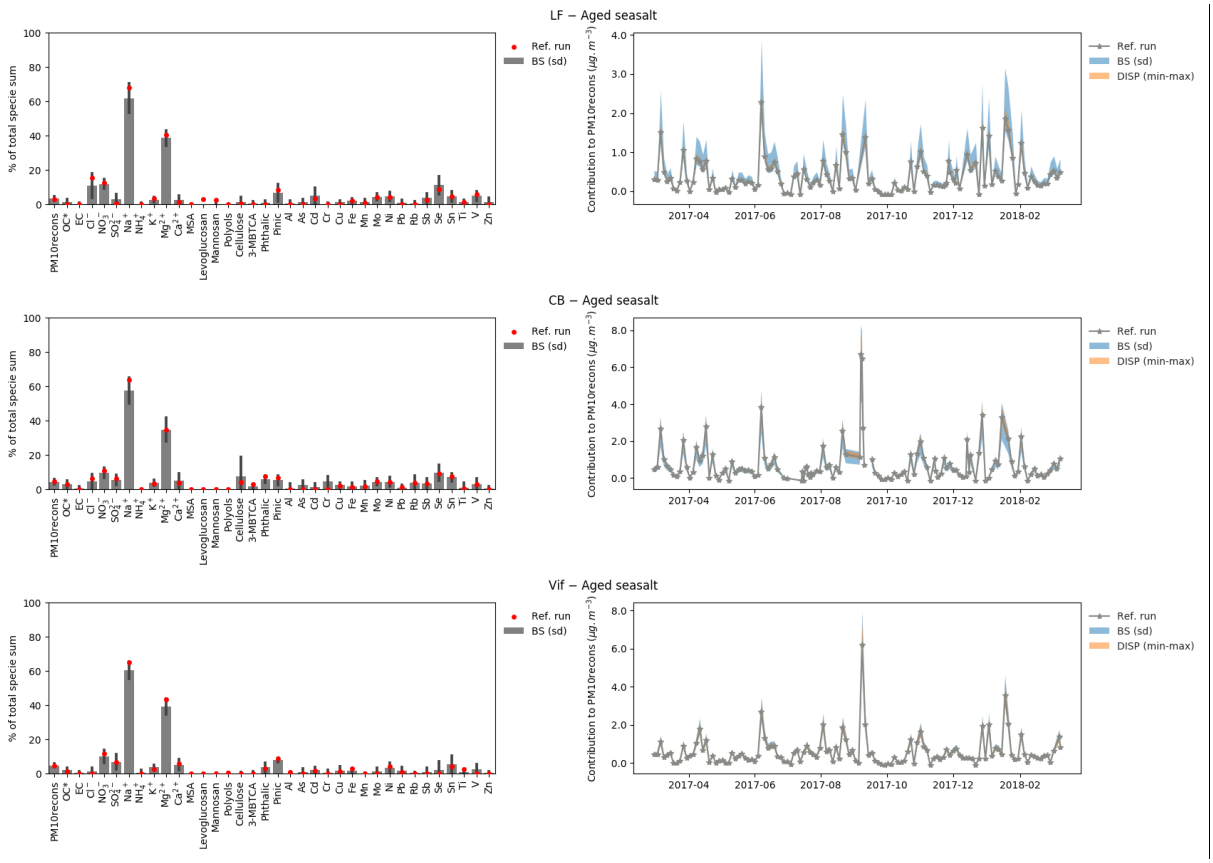

Figure S3.3. Chemical profile and temporal evolution with error estimates of the sea salt factor in LF (top), CB (middle), and Vif (bottom).

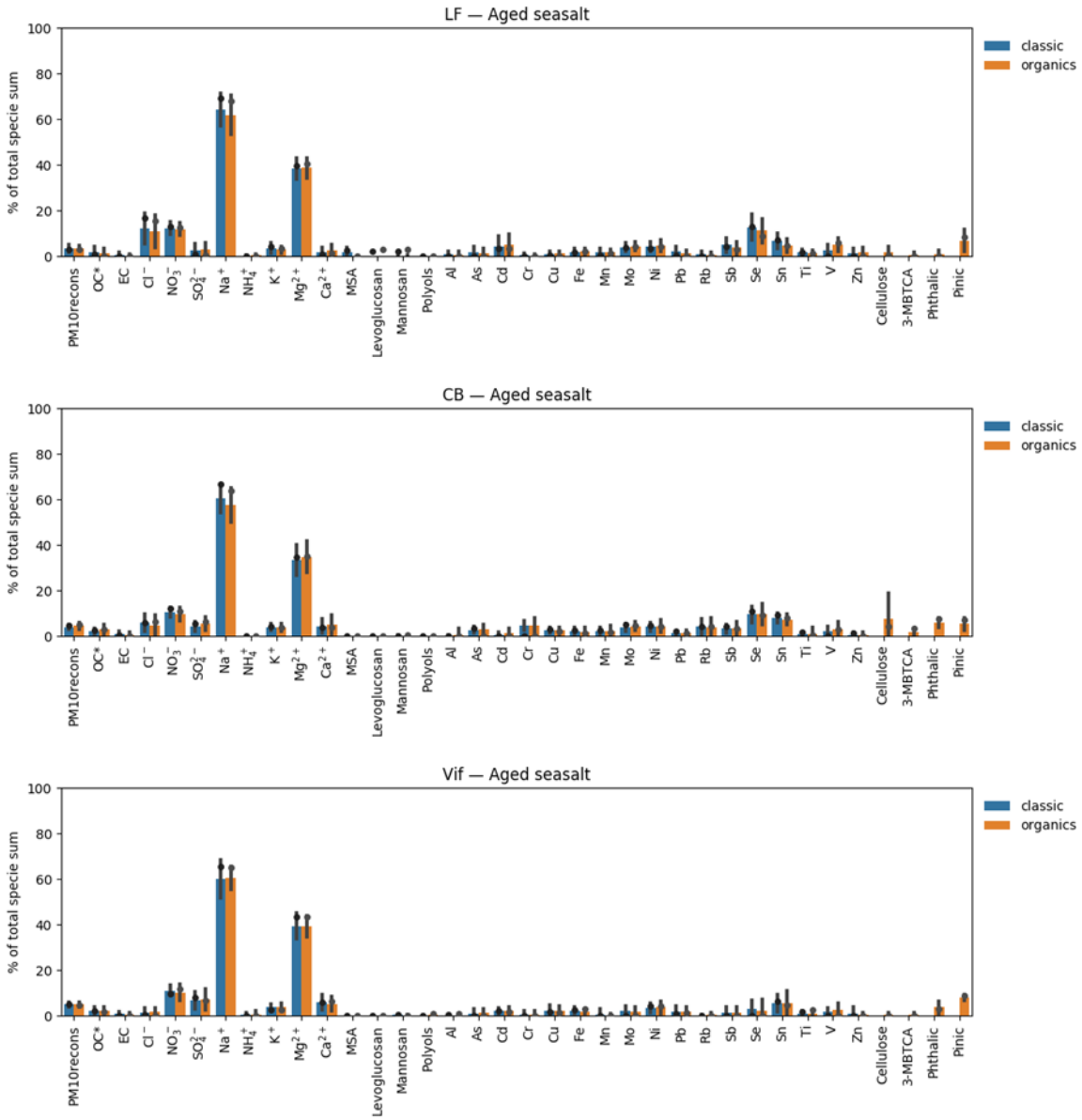

Figure S3.3.1 Comparison of chemical profile between the classic and orga PMF run for the aged sea salt factor in LF (top), CB (middle), and Vif (bottom).

See discussion of the Sea/road salt.

Sea/road salt

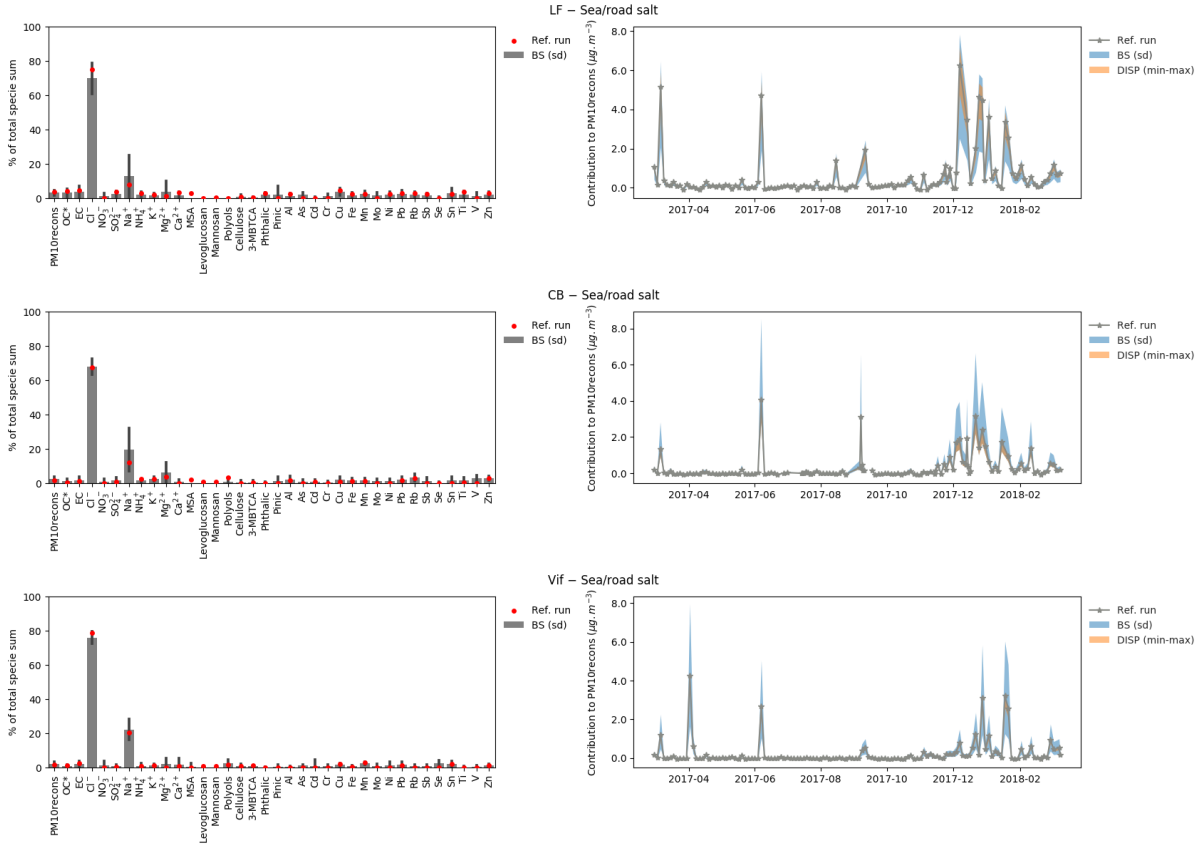

Figure S3.4. Chemical profile and temporal evolution with error estimates of the sea/road salt factor in LF (top), CB (middle), and Vif (bottom).

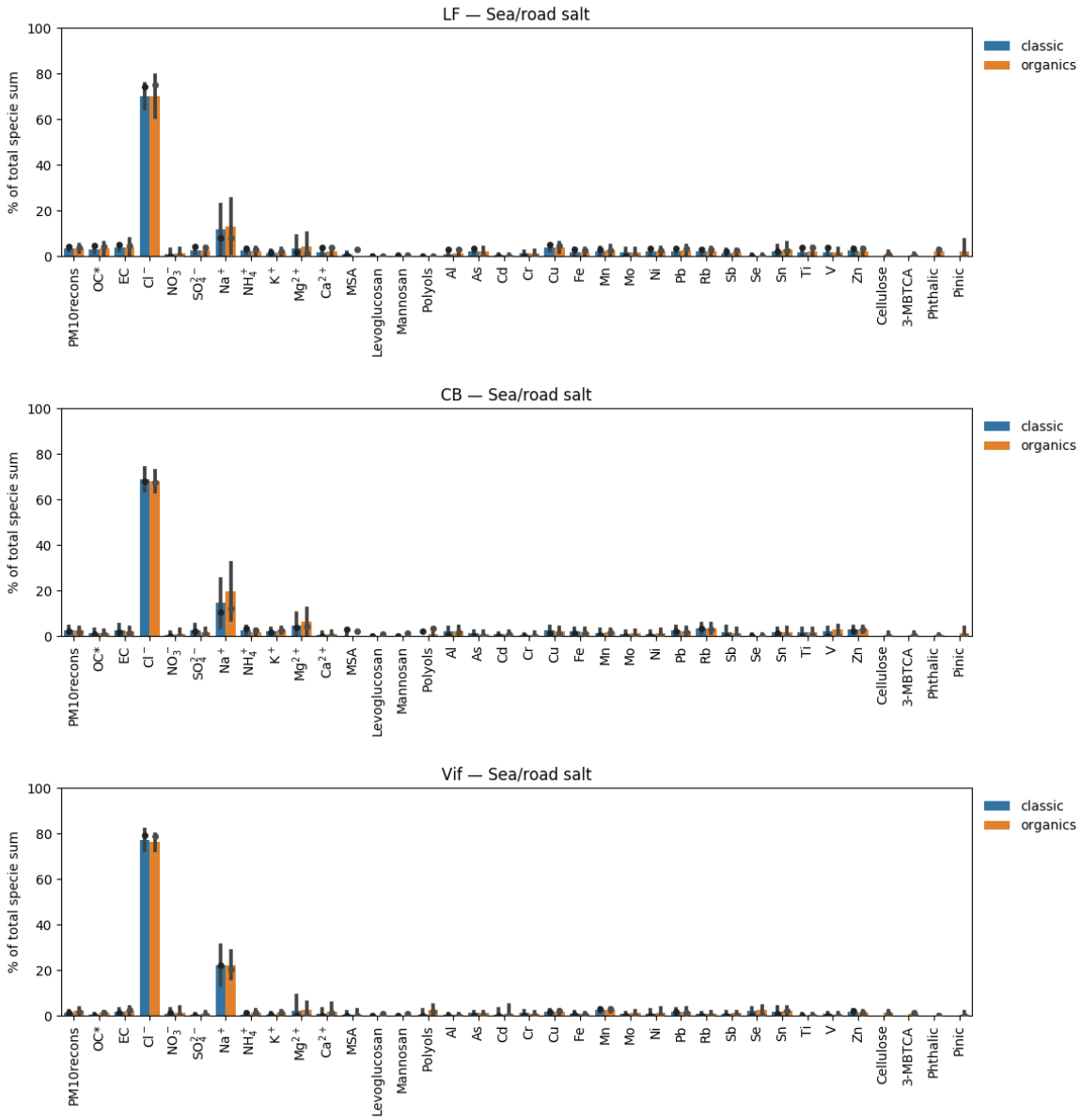

Figure S3.4.1 Comparison of chemical profile between the classic and orga PMF run for the sea/road salt factor in LF (top), CB (middle), and Vif (bottom).

The aged sea salt factor was identified with high loadings of Na^+ and Mg^{2+}. The strong correlations of ions across all sites have been reflected in the strong correlations found between sea salt factors across all sites. On an annual scale, sea salt sources accounted for 3-5% of the total PM_{10} mass with a steady seasonal contribution. The observed minimal loadings of Cl^- in the aged sea salt factor resulted from an ageing process by heterogeneous reactions between particulate sea salt and acidic compounds (e.g., nitric and sulfuric acid) (Seinfeld and Pandis, 2012). On the other hand, the sea/road salt factor was identified with high loadings of Na^+ and Cl^- accounting for 2-4% of the total mass of PM_{10}. This factor could be attributed to road salting during colder months as similarly reported by Pere´-Trepat et al. (2007) and Wåhlin et al. (2006) as contributions were also notably higher during winter season.

Nitrate-rich

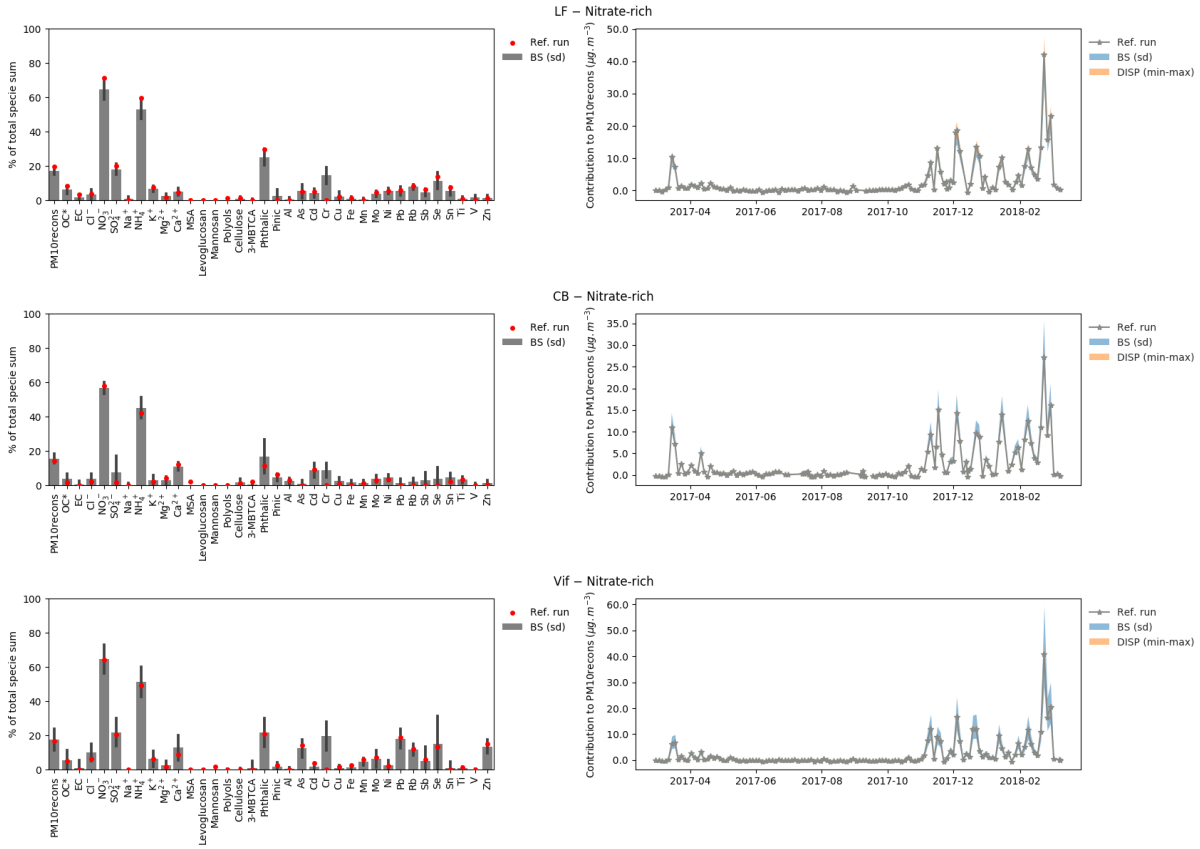

Figure S3.5. Chemical profile and temporal evolution with error estimates of the nitrate-rich factor in LF (top), CB (middle), and Vif (bottom).

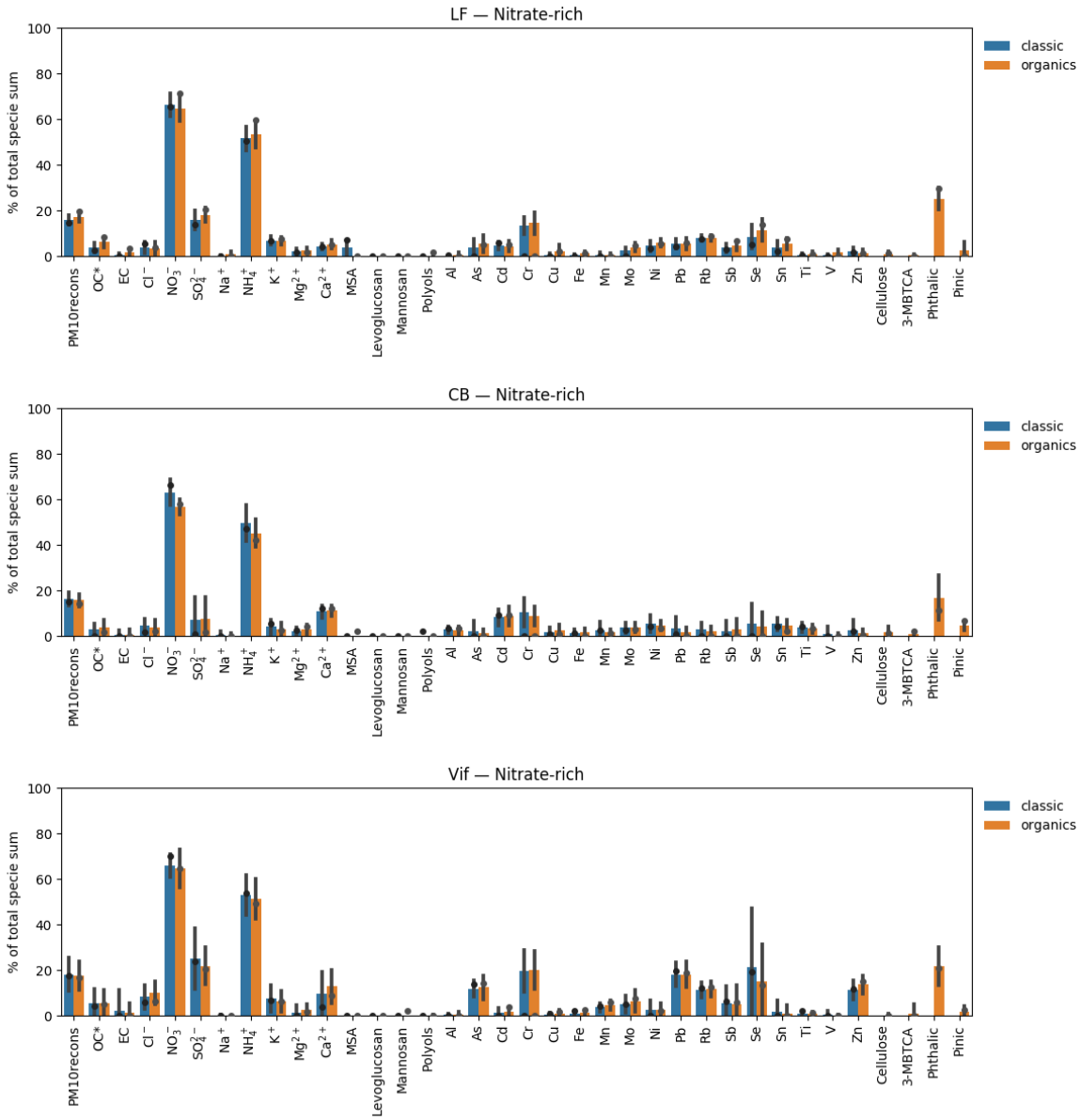

Figure S3.5.1 Comparison of chemical profile between the classic and orga PMF run for the nitrate-rich factor in LF (top), CB (middle), and Vif (bottom).

The nitrate-rich factor, a secondary aerosol source derived from the presence of NO_3NH_4 in the atmosphere, was identified with high loadings of NO_3^- and NH_4^+. The mass concentrations of these tracers have showed strong correlations across sites possibly indicating similar atmospheric process affecting the contributions of the nitrate-rich source of PM_{10} in the Grenoble basin. On an annual scale, nitrate-rich sources accounted for 14-19% of PM_{10} in all sites.

This factor showed strong seasonality with highest contributions during winter season which can be attributed to increased possibility of atmospheric inversions due to typical atmospheric dynamics during this season in the area. Additionally, this temporal behaviour can be due to higher instability of NO_3^- and NH_4^+ during warm seasons (Mariani and De Mello, 2007). These tracers are also commonly associated to secondary formation processes and long range transport of aged air masses especially during high PM_{10} concentration levels (Tomaz et al. 2017). The presence of phthalic acid in the nitrate-rich factor also suggests influence from SOA formation

(Al-Neima and Stone, 2017; Kleindienst et al, 2012). In fact, a high pollution event (PM_{10} ranging from 44.80-50.0 µg m^{-3}) affecting all the sites was noted during winter (February 23, 2018) where the concentrations of specific species including NO_3^-, SO_4^{2-}, NH_4^+, and phthalic acid were elevated in all sites. During this day, the nitrate-rich factor accounted for 83% (in LF), 50% (in CB), and 60% (in Vif) of the total PM_{10} confirming heavy influence of secondary formation processes possibly due to long range transport of pollutants.

Sulfate-rich

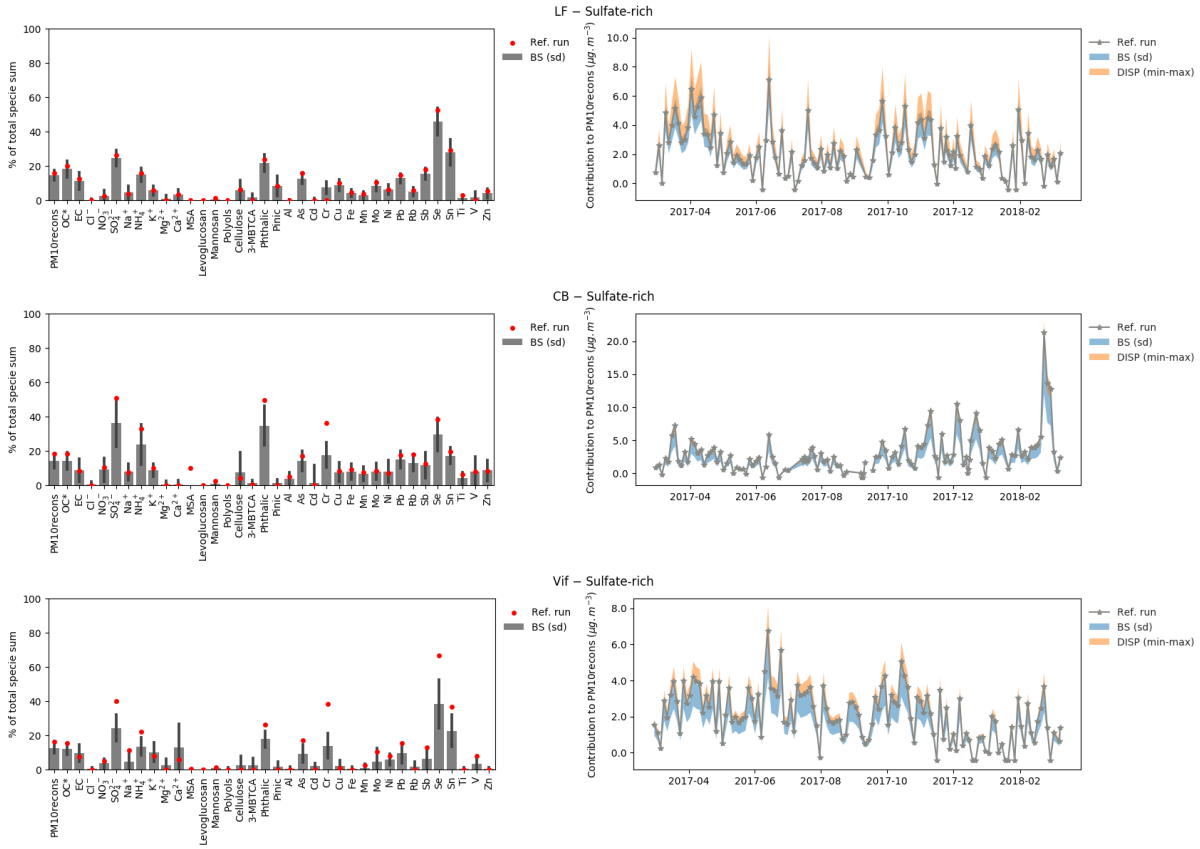

Figure S3.6. Chemical profile and temporal evolution with error estimates of the sulfate-rich factor in LF (top), CB (middle), and Vif (bottom).

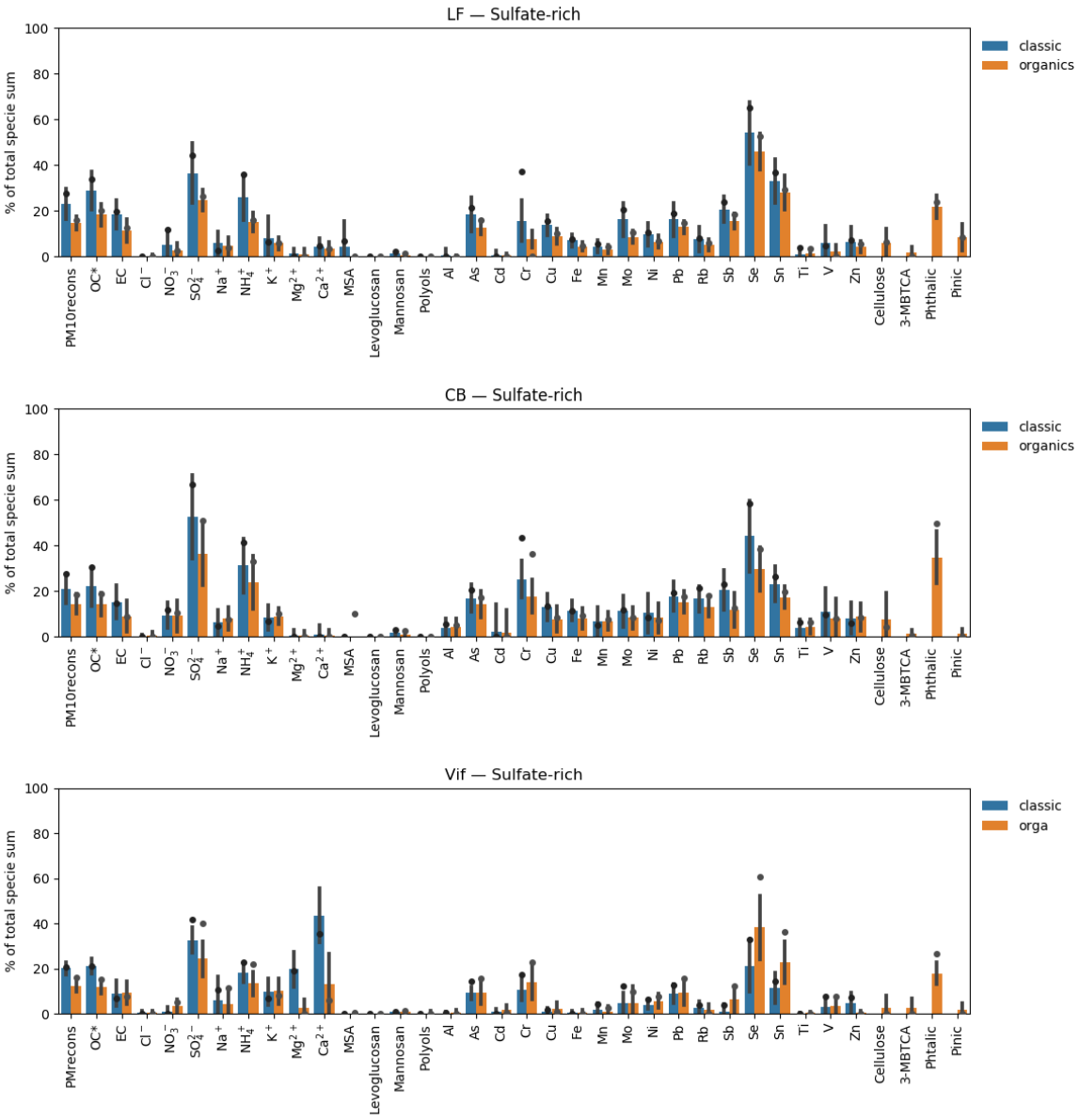

Figure S3.6.1 Comparison of chemical profile between the classic and orga PMF run for the sulfate-rich factor in LF (top), CB (middle), and Vif (bottom).

The sulfate-rich factor, a secondary aerosol source from $SO_4(NH_4)_2$, was identified with high loadings of SO_4^{2-}, NH_4^+, and Se. In Vif, this factor also had minimal loadings of metal species including Cr and Sn. On an annual scale, sulfate-rich factor accounted for 16-18% of PM_{10} across the urban sites in Grenoble.

This factor remained relatively steady due to the influence from long-range transport but did not show seasonality that was previously found in the nitrate-rich factor. Most of the tracers, SO_4^{2-}, NH_4^+, and phthalic acid, in this factor have showed strong correlations across sites, except for Se. The presence of Se in this factor may suggest a contribution from gasoline and diesel emissions (De Santiago et al., 2014) which can be highly localized in nature affecting the over-all temporal correlation of the sulfate-rich source across sites. The presence of phthalic acid in this factor also suggests influence from SOA formation as reported in other studies (Al-Neima and Stone, 2017; Kleindienst et al., 2012).

Primary biogenic

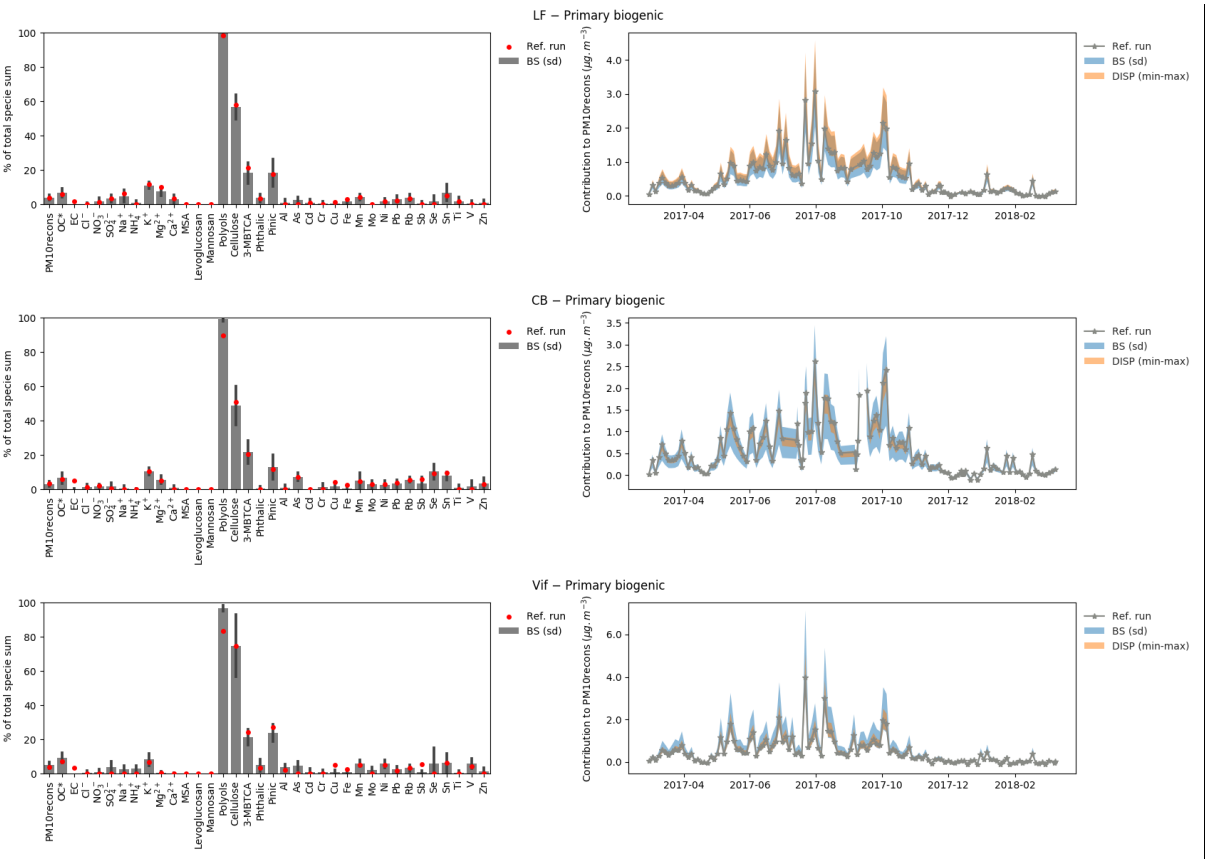

Figure S3.7. Chemical profile and temporal evolution with error estimates of the primary biogenic factor in LF (top), CB (middle), and Vif (bottom).

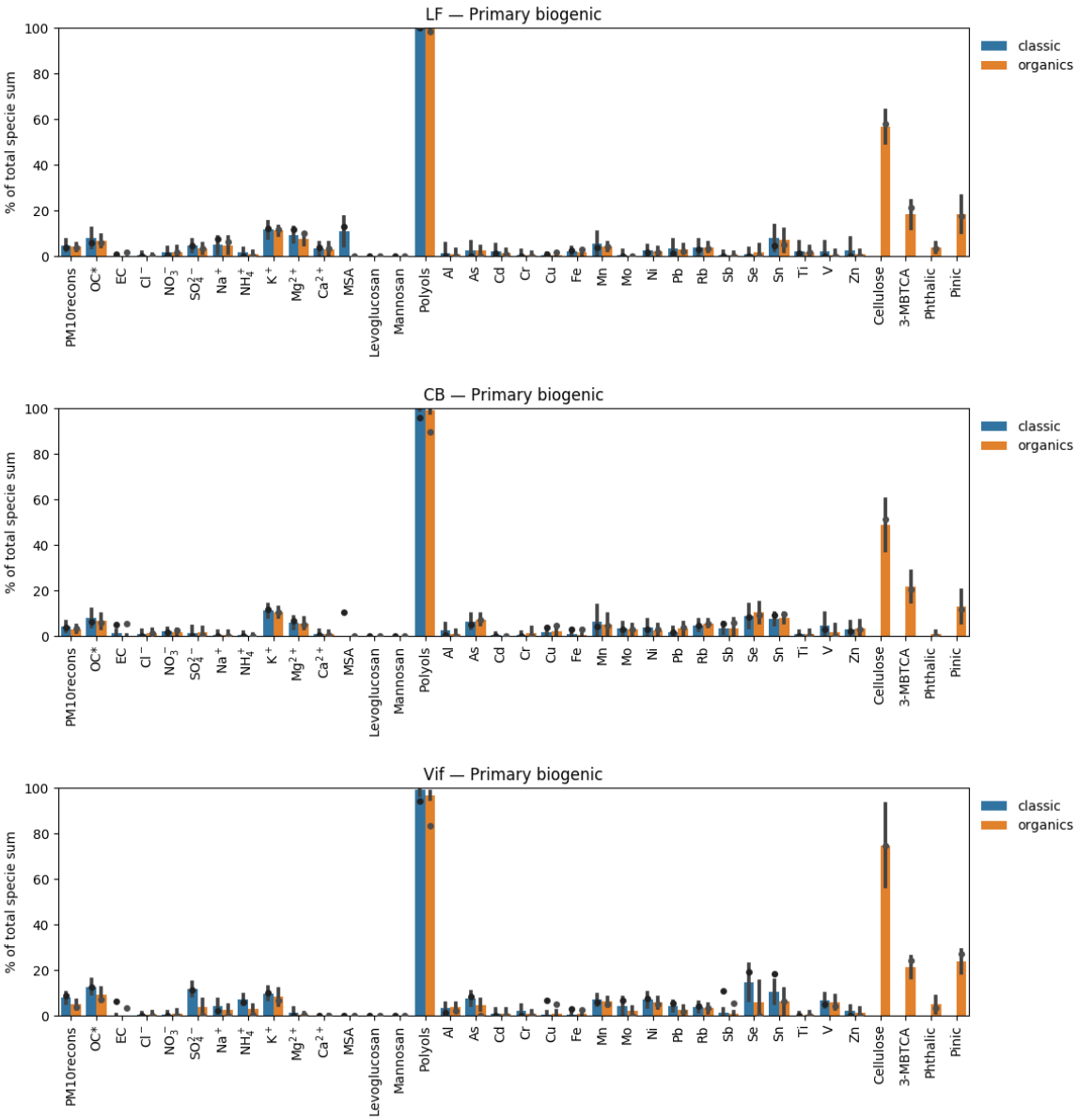

Figure S3.7.1 Comparison of chemical profile between the classic and orga PMF run for the primary biogenic factor in LF (top), CB (middle), and Vif (bottom).

MSA-rich

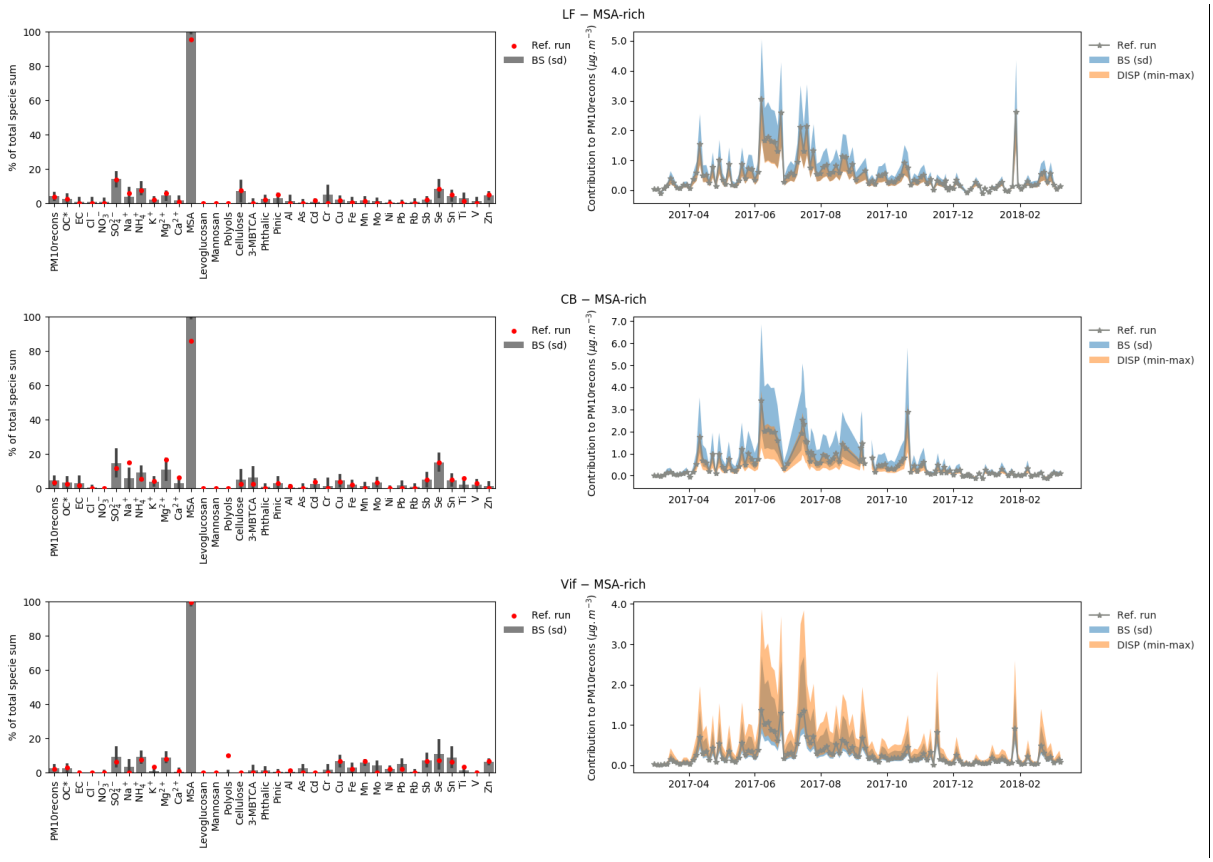

Figure S3.8. Chemical profile and temporal evolution with error estimates of the MSA-rich factor in LF (top), CB (middle), and Vif (bottom).

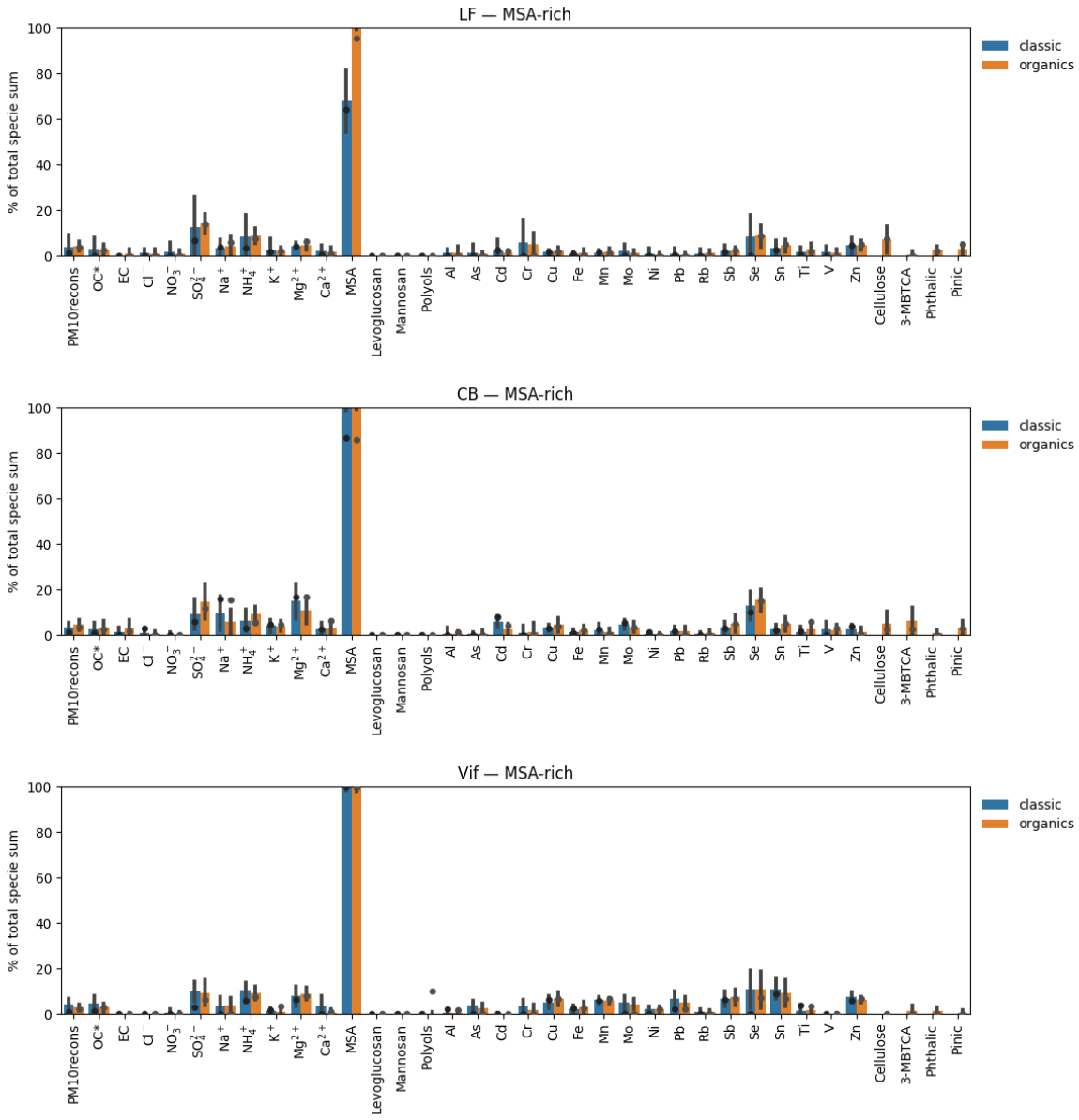

Figure S3.8.1 Comparison of chemical profile between the classic and orga PMF run for the MSA-rich factor in LF (top), CB (middle), and Vif (bottom).

Secondary biogenic oxidation

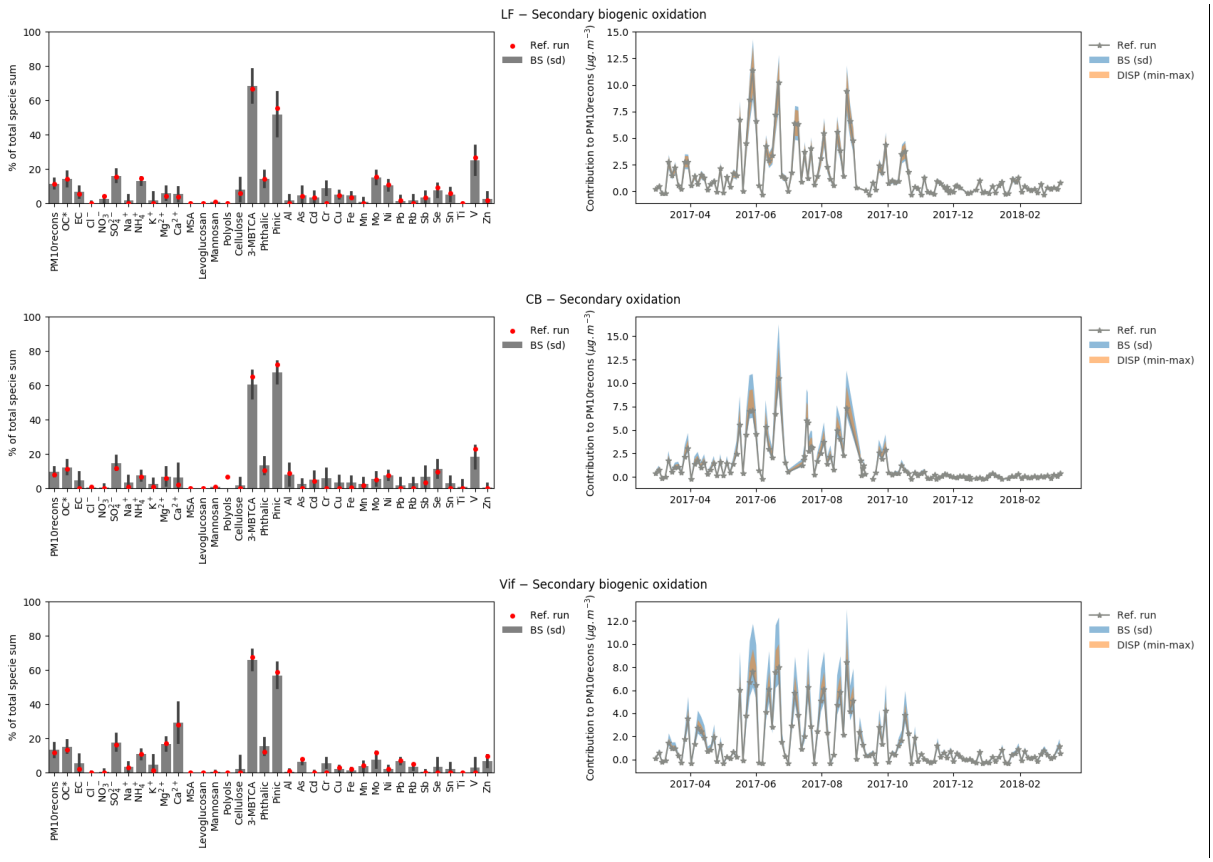

Figure S3.9. Chemical profile and temporal evolution with error estimates of the secondary biogenic oxidation factor in LF (top), CB (middle), and Vif (bottom). Note: This factor was not identified in the classic PMF run.

Industrial

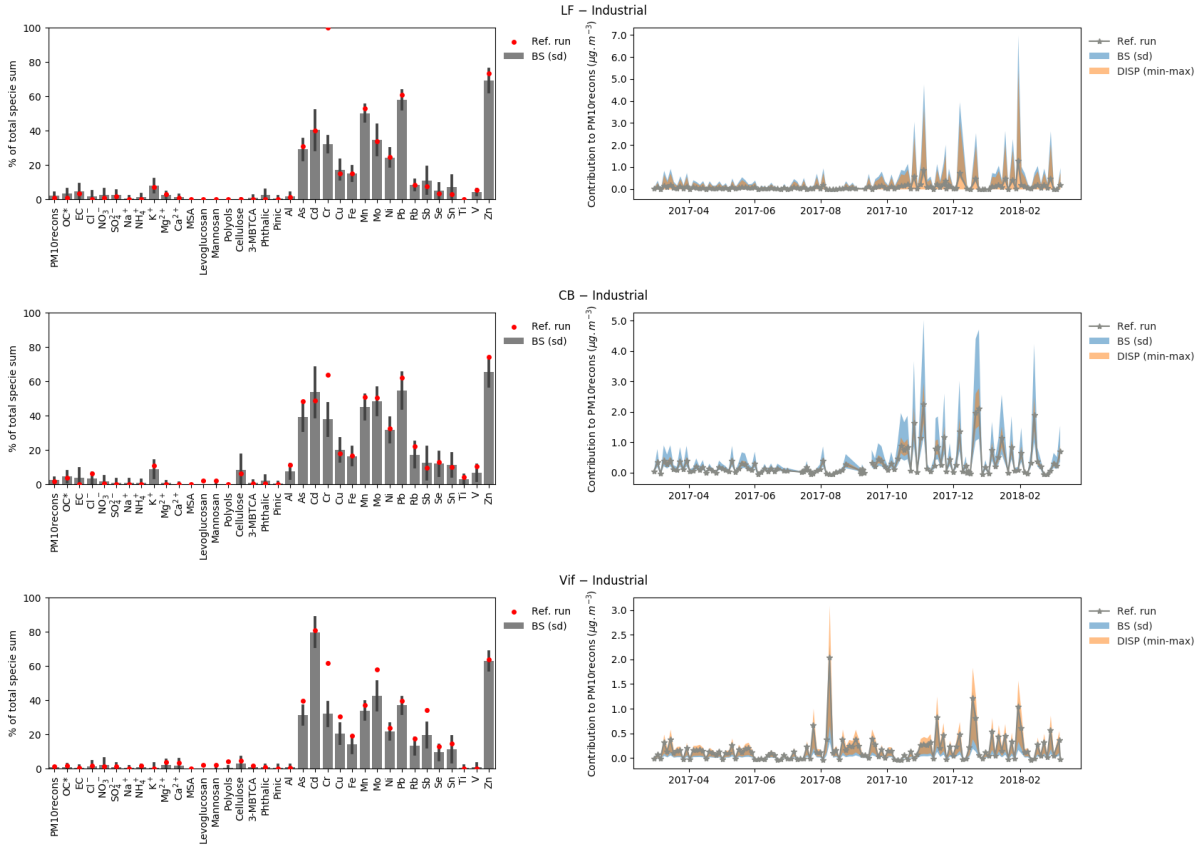

Figure S3.10. Chemical profile and temporal evolution with error estimates of the industrial factor in LF (top), CB (middle), and Vif (bottom)

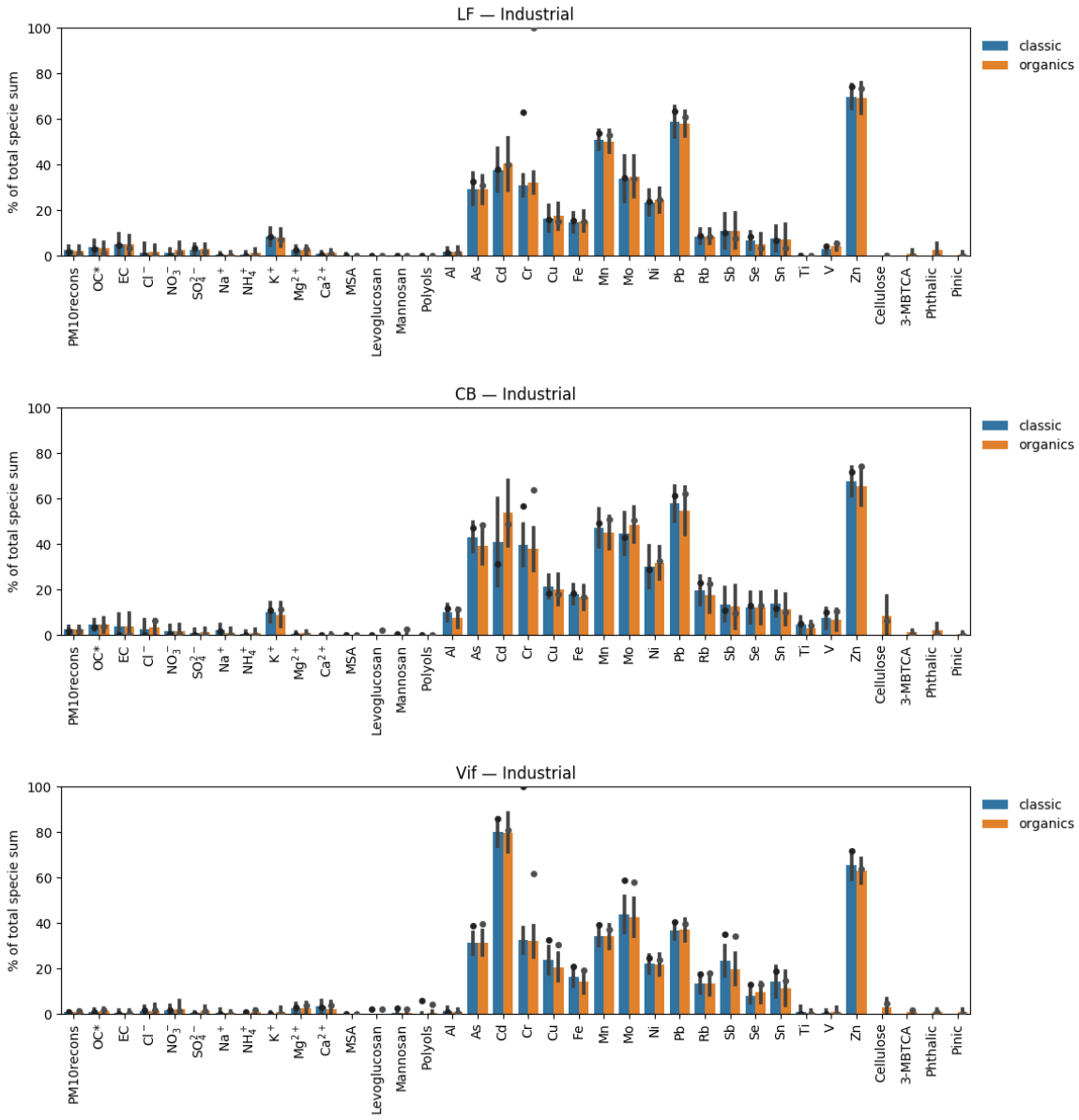

Figure S3.10.1 Comparison of chemical profile between the classic and orga PMF run for the industrial factor in LF (top), CB (middle), and Vif (bottom).

The industrial factor was identified with high loadings of trace elements including As, Cd, Cr, Mn, Mo, Ni, Pb, and Zn. On an annual scale, this factor only accounted for 1-2% of the total mass of PM. It is interesting to note that LF and CB showed comparable chemical profiles suggesting possible similarity in origin of this factor resulting to mild correlations between these two sites. However, only weak correlations were seen in the industrial factor when compared to Vif. In fact, Vif showed much higher contribution of Cd compared to other metals in this factor. Nevertheless, this further highlights the robustness of the PMF model in discriminating the chemical profiles of PM_{10} sources in spite of diversity at a fine-scale resolution.

One of the possible sources of Cd and Ni in the city of Grenoble are modern municipal waste incinerators (Boudet et al., 1999). The elevated contributions of Cd in Vif may also be due to additional influence from a nearby chemical industrial area (<6 km of the sampling location) in the southeast of Grenoble.

Mineral dust

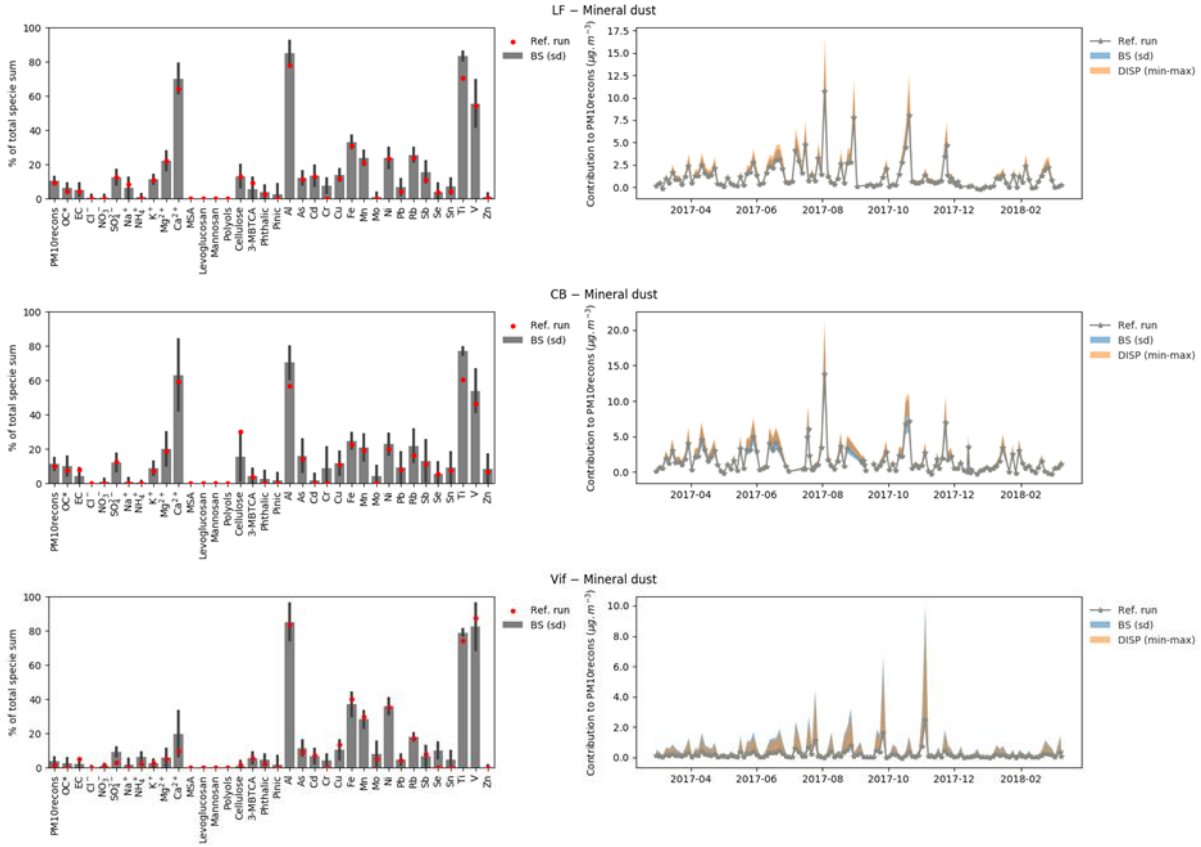

Figure S3.11. Chemical profile and temporal evolution with error estimates of the mineral dust factor in LF (top), CB (middle), and Vif (bottom).

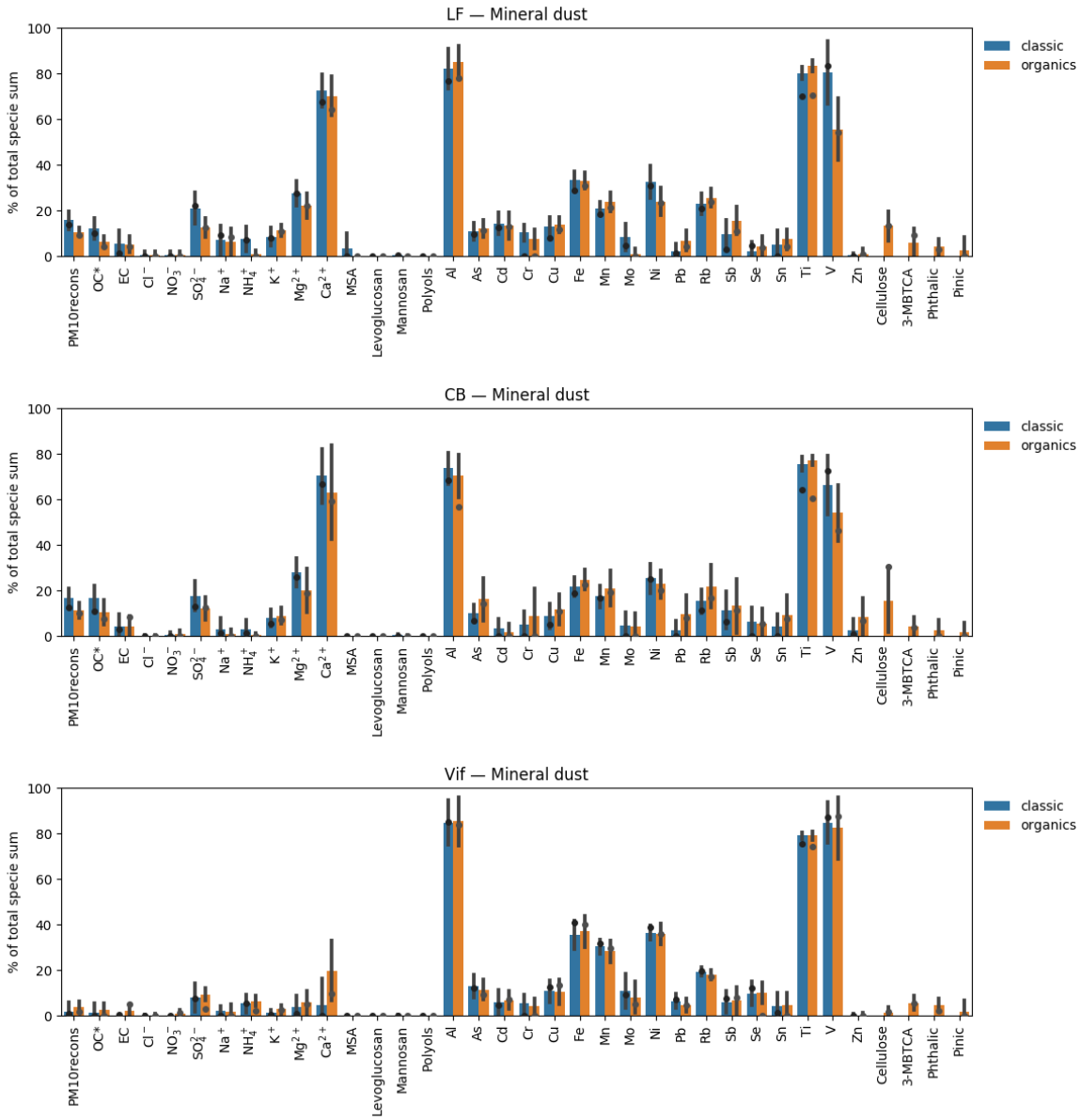

Figure S3.11.1 Comparison of chemical profile between the classic and orga PMF run for the mineral dust factor in LF (top), CB (middle), and Vif (bottom).

The mineral dust factor was identified with high loadings of Ca^{2+}, Al, Ti, and V. In Vif, this factor did not show as much loading of Ca^{2+} (see Fig. S3.11). The temporal evolution of Ca^{2+} showed strong correlations across all sites, however good correlations from Al, Ti, and V were only found between LF and CB which has further resulted to strong correlations of the mineral dust factor in these two sites. This highlights the capability of PMF to analyse and differentiate the chemical profiles of sources even at high proximity of receptor locations. The loadings from metal tracers suggests natural dust, and fossil fuel or industrial origins of this factor, especially in Vif (Luo et al., 2008; Pan et al., 2015).

The presence of Fe, a good indicator of road traffic emissions, also suggests possible influence from road dust resuspension in the mineral dust factor. On an annual scale, mineral dust sources accounted for 9%, 10%, and 2% in LF, CB, and Vif, respectively.

S4. Comparison between the PMF results from Srivastava et al. (2018b) and our study

One of the sites in our study, LF (urban background site), has been previously reported using a one-year dataset collected in year 2013 (Srivastava et al., 2018b). The comparison of PMF results obtained including the sources and its corresponding tracers and percentage contribution are summarized in Table S4.

However, there are some differences in the input variables used resulting to differences in the identified sources. The sources that are common to both studies are biomass burning, primary traffic, mineral dust, and aged sea salt. The nitrate-rich and sulfate-rich sources were obtained separately in our study while it was combined into one factor as the secondary inorganics in Srivastava et al. (2018b). Although the tracers are available, sea/road salt and industrial sources were not identified in Srivastava et al. (2018b). Due to the specific organic tracers used in our study, we have also additionally obtained primary biogenic, MSA-rich, and secondary biogenic oxidation sources.

It should be noted that Srivastava et al. (2018b) have identified a fungal spores source identified by high loadings of polyols, which is one of the tracers that was similarly used to identify the primary biogenic source in our study. This is only a question of naming the profile, fungal spores emissions being one type of primary biogenic emissions. On the other hand, the plant debris factor (another type of primary biogenic emissions) from their study using alkane tracers were considered to be accounted in the primary biogenic factor in our study through the contributions of cellulose in this factor. Although different organic acids were used, Srivastava et al. (2018b) was able to obtain a biogenic SOA source identified by contributions from α-methylglyceric acid (α-MGA and 2-methylerythritol (2-MT), hydroxyglutaric acid (3-HGA), while our study have obtained a secondary biogenic oxidation source identified by 3-MBTCA and pinic acid. Both of these factors are identified as a secondary biogenic oxidation source and are very close in terms of percentage contribution. Lastly, Srivastava et al. (2018b) was able to obtain an anthropogenic SOA source that was not identified in our study but may be considered to be mixed in multiple sources through the contributions of phthalic acid.

Table S4. The comparison of PMF-resolved sources, tracers, and annual average percentage contribution between Srivastava et al. (2018b) and our study.

Sources	Our study (LF only)			Srivastava et al. (2018b)	
	Tracers	Percentage contribution (%)	Average±std (μg m^{-3})	Tracers	Percentage contribution (%)
Biomass burning	Levoglucosan, mannosan, K^+, Rb, Cl^-	17	2.3±3.2	Levoglucossan, coniferaldehyde, vanillic acid	20
Primary traffic	EC, Ca^{2+}, Cu, Fe, Sb, Sn	12	1.8±2.4	EC, hopanes (H5 to H8)	14
Nitrate-rich	NO_3^-, NH_4^+	20	2.8±5.7	N/A	N/A
Sulfate-rich	SO_4^{2-}, NH_4^+, Se	16	2.2±1.6	N/A	N/A
Mineral dust	Ca^{2+}*, Al, Ti	9	1.3±1.6	Ca, Al, Ti	21
Sea/road salt	Na^+, Cl^-	4	0.5±1.1	N/A	N/A
Aged sea salt	Na^+, Mg^{2+}	3	0.4±0.4	Na^+, Mg^{2+}	2

Industrial	As, Cd, Cr, Mn, Mo, Ni, Pb, Zn	1	0.1±0.2	N/A	N/A
Primary biogenic	Polyols, cellulose	4	0.5±0.6	N/A	N/A
MSA-rich	MSA	4	0.5±0.6	N/A	N/A
Secondary biogenic oxidation	3-MBTCA, pinic acid	11	1.6±2.3	N/A	N/A
Fungal Spores	N/A	N/A	N/A	Polyols	5
Secondary inorganics	N/A	N/A	N/A	NO_3^-, $NH_4^{+,}$, $SO4^{2-}$, Cl^-	13
Plant debris	N/A	N/A	N/A	alkanes (C27 to C31)	11
Biogenic SOA	N/A	N/A	N/A	α-methylglyceric acid (α-MGA and 2-methylerythritol (2-MT), hydroxyglutaric acid (3-HGA)	12
Anthropogenic SOA	N/A	N/A	N/A	acenaphthenequinone, 6H–dibenzo[b,d]pyran-6-one, 1,8-naphthalic anhydride, DHOPA	2

Note: N/A: not available

S5. Scatterplot of factor contributions site vs site

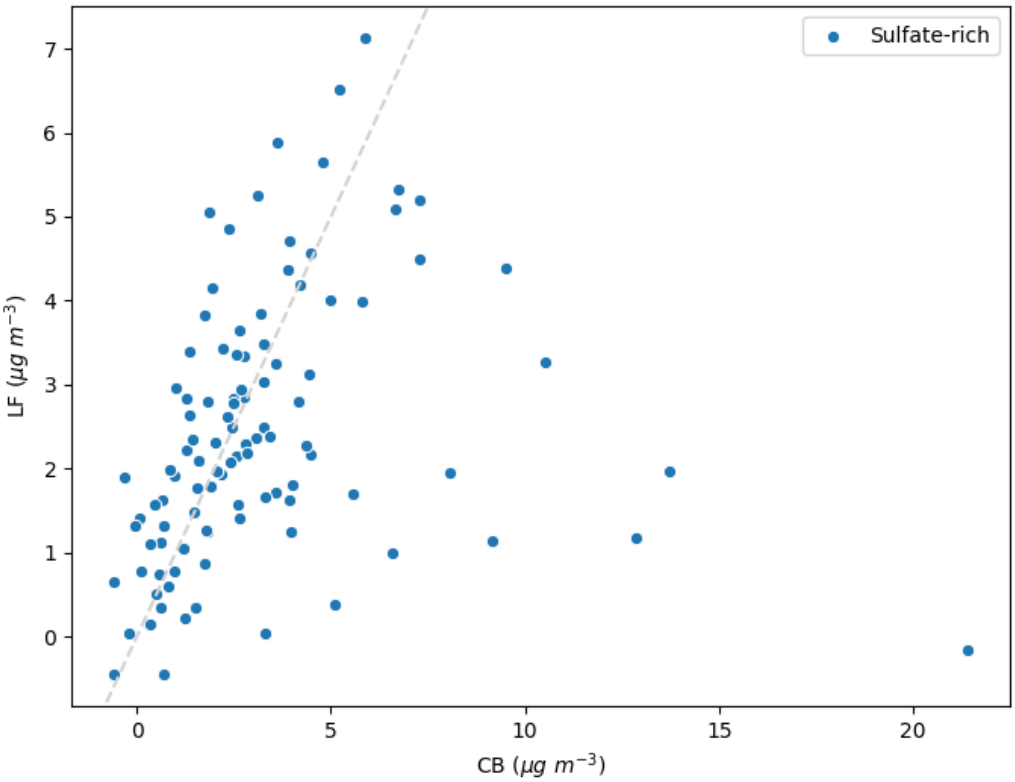

Figure S5.1. Scatterplot of the sulfate-rich factor contribution between CB and LF. The dotted line is the x=y line.

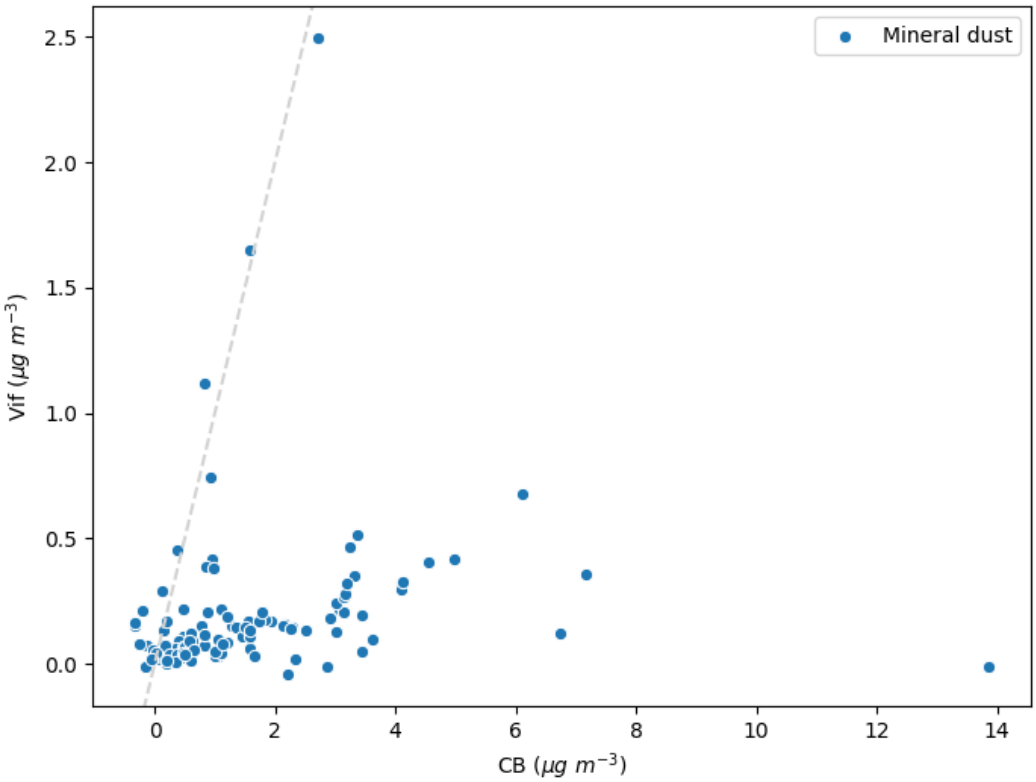

Figure S5.2. Scatterplot of the mineral dust factor contribution between CB and Vif. The dotted line is the x=y line.

S6. Comparison of chemical profiles from this study and from the 15 French sites (SOURCES)

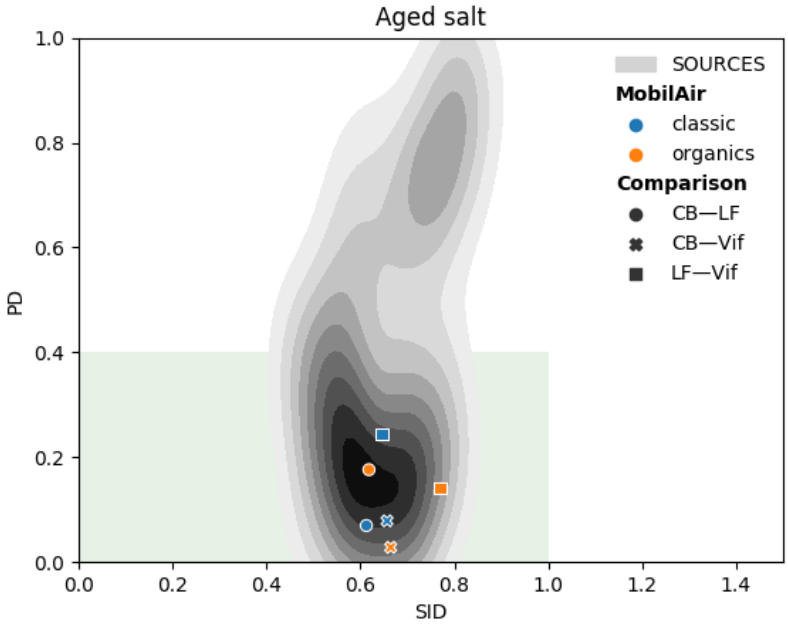

Figure S6.1: Similarity plots for the aged sea salt factor for the pairs of sites formed in this study (Mobil'Air) compared to the probability density function of similarities obtained for the 15 French sites of the SOURCES program.

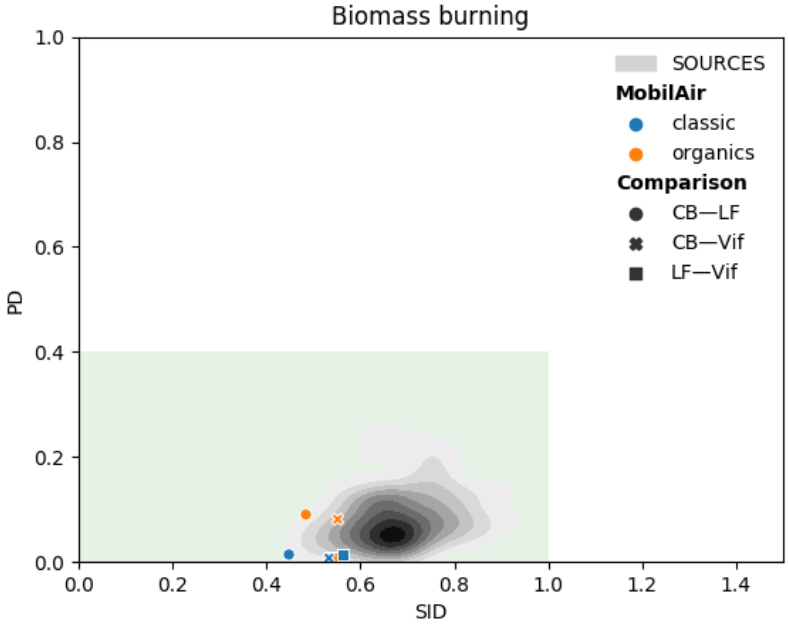

Figure S6.2: Similarity plots for the biomass burning factor for the pairs of sites formed in this study (Mobil'Air) compared to the probability density function of similarities obtained for the 15 French sites of the SOURCE program.

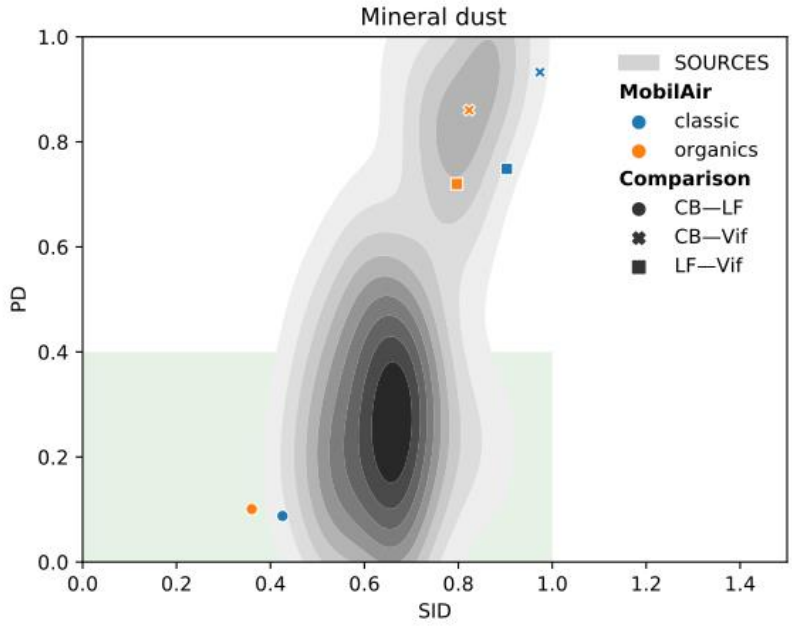

Figure S6.3: Similarity plots for the mineral dust factor for the pairs of sites formed in this study (Mobil'Air) compared to the probability density function of similarities obtained for the 15 French sites of the SOURCES program.

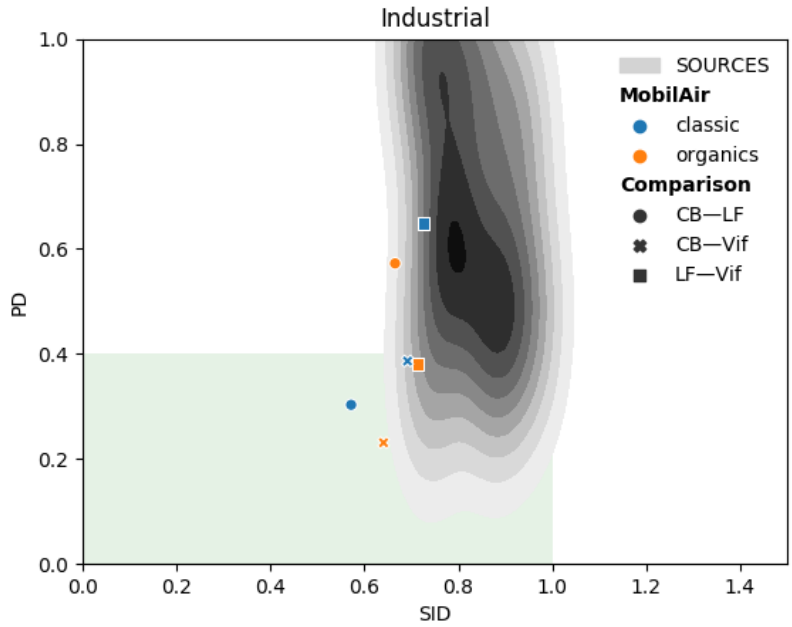

Figure S6.4: Similarity plots for the industrial factor for the pairs of sites formed in this study (Mobil'Air) compared to the probability density function of similarities obtained for the 15 French sites of the SOURCES program.

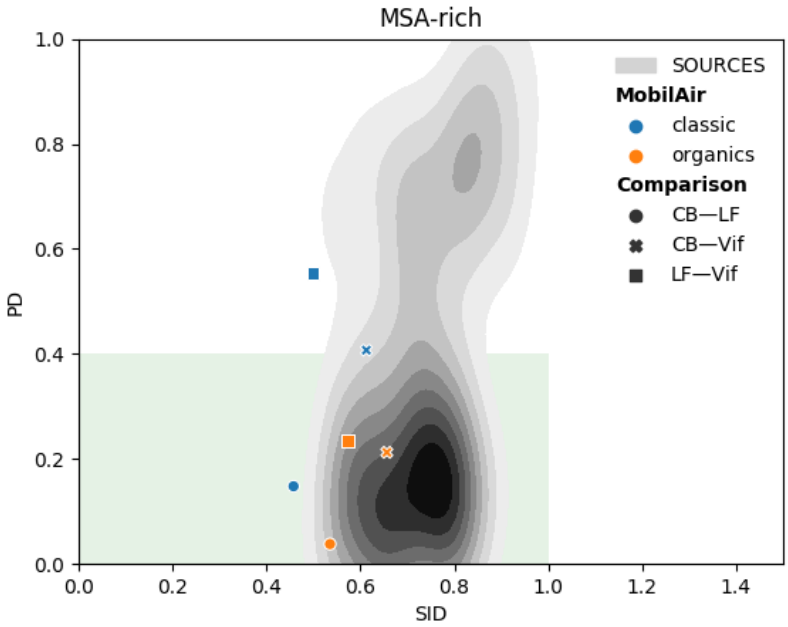

Figure S6.5: Similarity plots for the MSA-rich factor for the pairs of sites formed in this study (Mobil'Air) compared to the probability density function of similarities obtained for the 15 French sites of the SOURCES program.

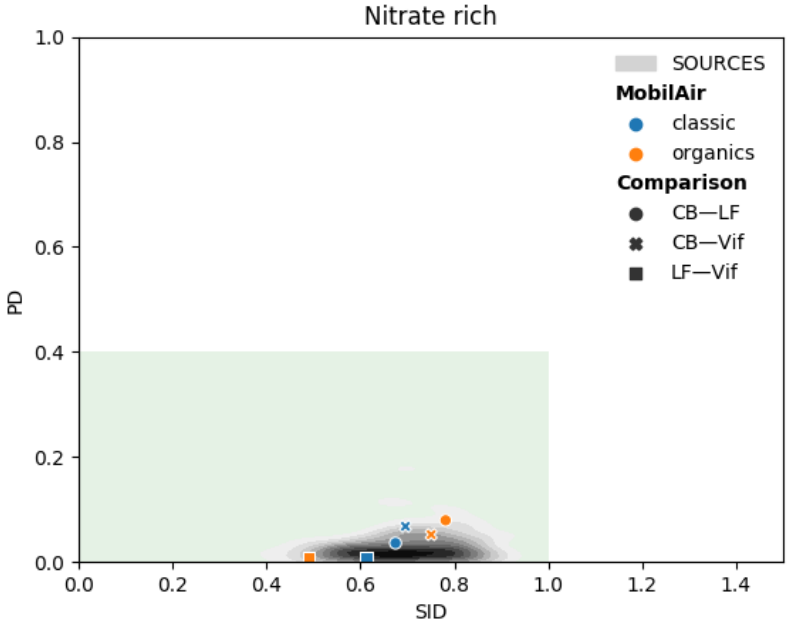

Figure S6.6: Similarity plots for the nitrate-rich factor for the pairs of sites formed in this study (Mobil'Air) compared to the probability density function of similarities obtained for the 15 French sites of the SOURCES program.

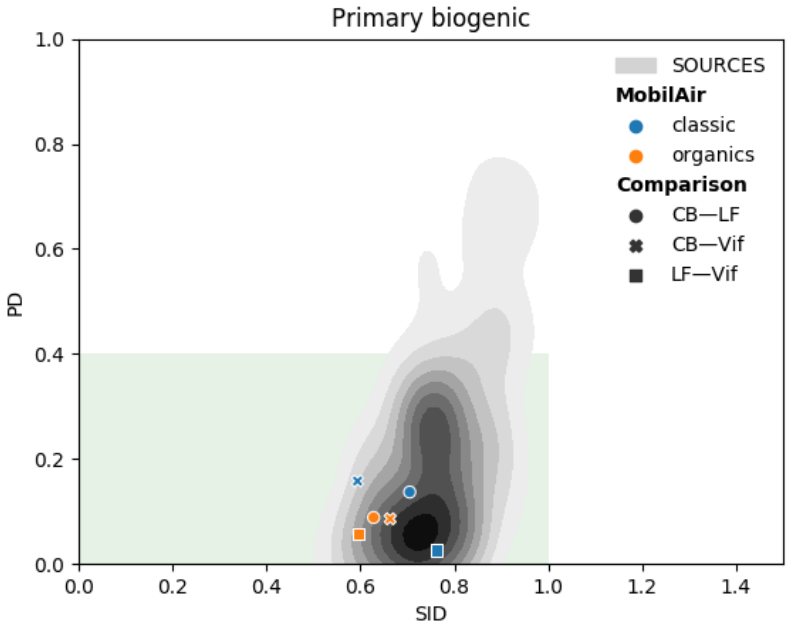

Figure S6.7: Similarity plots for the primary biogenic factor for the pairs of sites formed in this study (Mobil'Air) compared to the probability density function of similarities obtained for the 15 French sites of the SOURCES program.